Constitutive and Fracture Characterization of an Anisotropic and Asymmetric Alloy Sheet

by

Armin Abedini

A thesis

presented to the University of Waterloo

in fulfillment of the

thesis requirement for the degree of

Doctor of Philosophy

in

Mechanical and Mechatronics Engineering

Waterloo, Ontario, Canada, 2018

EXAMINING COMMITTEE MEMBERSHIP

The following served on the Examining Committee for this thesis. The decision of the Examining Committee is by majority vote.

Supervisors	Michael Worswick, Ph.D.
	Professor, University of Waterloo
	Clifford Butcher, Ph.D.
	Assistant Professor, University of Waterloo
External Examiner	Krishnaswamy Ravi-Chandar, Ph.D.
	Professor, University of Texas at Austin
Internal Examiner	Kaan Inal, Ph.D.
	Associate Professor, University of Waterloo
Internal Examiner	Kamyar Ghavam, Ph.D.
	Lecturer, University of Waterloo
Internal-External Examiner	Robert Gracie, Ph.D.
	Associate Professor, University of Waterloo

AUTHOR'S DECLARATION

This thesis consists of material all of which I authored or co-authored (see Statement of Contributions included in the thesis).

This is a true copy of the thesis, including any required final revisions, as accepted by my examiners.

I understand that my thesis may be made electronically available to the public.

STATEMENT OF CONTRIBUTIONS

The following co-authors have contributed to the current work:

Professor Michael Worswick and Professor Cliff Butcher supervised this Ph.D. thesis.

Dr. Michael Nemcko performed the X-Ray Diffraction (XRD) and Electron Backscattered Diffraction (EBSD) analyses.

Dr. Srihari Kurukuri assisted with preparing compression specimens and performing compression tests.

The balance of the research is my own work.

ABSTRACT

Magnesium alloys can offer significant weight reduction over conventional steel or aluminum alloys. Specifically, rare-earth alloyed magnesium sheets have the potential to be used as light-weight structural alloys since they possess a weakened crystallographic texture that leads to superior ductility over conventional magnesium alloys. However, there are some complications that limit wide-spread adoption of these alloys that are mainly attributed to their significant anisotropy and complex yielding behaviour, as well as their limited ductility (relative to cubic materials) and their orientation-dependent fracture response. The present thesis aims to address some of these challenges to support the commercial implementation of these alloys.

Examining ZEK100-O rare-earth magnesium rolled sheet as a model material, the constitutive plastic and fracture behaviour of the alloy were characterized to reveal the response of the material under different quasi-static loading conditions at room temperature. Given the complex yielding behaviour of the material, a continuum-based plasticity model has been developed that captures evolving anisotropy and tension-compression asymmetry of ZEK100-O. The modelling framework consists of the CPB06 yield criterion for hcp materials along with a non-associative flow rule in which the yield function and plastic potential were calibrated for a range of plastic deformation levels along with an interpolation approach to account for evolving anisotropy under proportional loading conditions. The constitutive model has been implemented as a user material subroutine (UMAT) into the commercial finite element code, LS-DYNA, for general 3-D stress states. It is shown that predictions of the model were in good agreement with experimental data in terms of both global load-displacement as well as and local strain responses.

In addition to a remarkable anisotropy and symmetry in the plastic response of the material, fracture experiments in different test orientations revealed that the fracture behaviour of the material is also anisotropic. However, orientation-dependency in fracture is not as significant as anisotropy in plastic response. In order to visualize directional dependency of the fracture response of the magnesium alloy, experimental fracture *loci* for different orientations were constructed. Furthermore, non-proportional tests were performed incorporating abrupt changes in stress state to study the role of the loading history on fracture behaviour of the alloy. It is shown that simple damage indicators might not be able to capture accurately fracture response of the material under severe changes in the stress states.

ACKNOWLEDMENTS

First of all, I would like to thank Professor Michael Worswick for providing me with the opportunity to work on such an excellent project. I wish to express my sincere appreciation to him for abundant support, encouragement, and mentorship. In addition to learning from his exceptional knowledge, I am very fortunate to have a supervisor who has taught me many life lessons. I am very proud that I have had the honor of working under his supervision.

Also, this work was not possible without valuable guidance of my co-supervisor, Professor Cliff Butcher. I am grateful for his enthusiasm, patience, and support. His mentorship was not limited to my four years of Ph.D. studies. He taught me how to achieve the highest levels of academic excellence. I am very proud of our work together in the past six years.

To my parents: Ali and Azam

Table of Contents

LIST OF FIGURES

Synopsis of Thesis

1. Introduction

In recent years, there has been an increasing demand to reduce vehicle weight to tackle the global issue of green-house emissions and to meet stricter governmental regulations. Vehicle weight reduction is possible through the application of high strength materials such as advanced high strength steels (AHSS) or low density alloys like aluminum or magnesium. Magnesium is the lightest of all structural metals (Mordike and Ebert, 2001) with a density of approximately one-fourth of steel and two-thirds of aluminum that can offer great weight reduction relative to other materials. Wrought magnesium, particularly in the form of sheet, represents a tremendous growth opportunity in automotive applications such as inner door panel, engine hood, seat components, roof, and fenders (Zarandi and Yue, 2011).

Although magnesium alloys are attractive for vehicle light-weighting, the current actual application of magnesium alloys in automobiles is limited to approximately 1% of the average automobile by weight (Kim, 2014). High cost, poor formability at room temperature, and poor corrosion resistance are the most important drawbacks limiting widespread application of magnesium alloys. The crystal structure of magnesium is hexagonal close packed (hcp) which limits its inherent ductility, and efforts to produce alloys lead to preferred microstructural textures and severe plastic anisotropy. The future adoption of magnesium alloys in the automotive industry will depend upon how the above challenges are addressed.

The present thesis aims to characterize the anisotropic constitutive behaviour of materials displaying strong anisotropy and yield-asymmetry, using ZEK100-O magnesium alloy sheet as a model material. This thesis has been written in a manuscript-based style that consists of different parts. The first part includes the synopsis of the thesis containing a review of the current state of the art in characterization of the mechanical behaviour and modelling the response of anisotropic-asymmetric materials followed by a statement of the objectives of this research. Subsequently, major results and overall conclusions of the research are provided within this synopsis. A more detailed presentation of the methodology and results of this research follows in Appendices A, B, C, and D which are four published or submitted peer-reviewed manuscripts.

This research has provided modelling tools and material data needed to support the commercial adoption of complex materials such as magnesium alloys within automotive body panels and structures.

2. Literature Review

2.1. Magnesium Alloys

Where weight reduction is desired, such as in automotive applications, magnesium alloys can offer high strength-to-weight ratios. Among different grades of magnesium alloys, AZ31B with a nominal composition of Mg-3wt%Al-1wt%Zn currently has the highest number of applications (Zarandi and Yue, 2011); however, low ductility and corrosion resistance limit widespread applications of the alloy. To address the formability issue, the addition of rare-earth (RE) alloying elements emerged as a potential solution to increase ductility while preserving the low density of magnesium alloys (Kim, 2014; Imandoust *et al.*, 2017). The role of the RE elements in magnesium alloys is to randomize the crystallographic texture and improve the formability of the material. ZEK100-O is a RE magnesium alloy that exhibits a relatively weaker texture compared to the more common commercial AZ31B magnesium. The role of texture on the mechanical behaviour of materials is discussed further below.

The low ductility of magnesium rolled sheets is attributed to the hexagonal close packed (hcp) crystal structure along with significant plastic anisotropy as a result of preferred textures developed during rolling processes. In general, materials with the hcp structure have limited available deformation mechanisms to accommodate plastic straining at room temperature. The dominant deformation system of magnesium alloys at room temperature is slip on the basal plane (see Figure 2.1). Other non-basal slip systems (slip on prismatic and pyramidal planes) are also observed in magnesium alloys but require higher stresses to be activated (Lou *et al.*, 2007). In addition, magnesium rolled sheets exhibit complex anisotropic and tension-compression asymmetric responses (Ghaffari Tari *et al.*, 2014; Kurukuri *et al.*, 2014a,b; Steglich *et al.*, 2016; Habib *et al.*, 2017). The asymmetric behaviour is primarily due to the twinning mechanisms that provide independent deformation mechanisms (Lou *et al.*, 2007), but are highly sensitive to loading direction (Plunkett *et al.*, 2008; Qiao *et al.*, 2017). The most common twining modes in magnesium alloys are tensile twinning, compressive twinning, and secondary/double twinning as described by Qiao *et al.* (2017).

c

(1̄101) **c**

(1̄100)

c

a₃

[112̄0] **a₂**

a₁ (0001)

a₃

[112̄0] **a₂**

a₁

a₃

[112̄0] **a₂**

a₁

Basal-< **a** >
(0001) < 112̄0 >, 3

Prismatic-< **a** >
{101̄0} < 112̄0 >, 3

Pyramidal-< **a** >
{101̄1} < 112̄0 >, 6
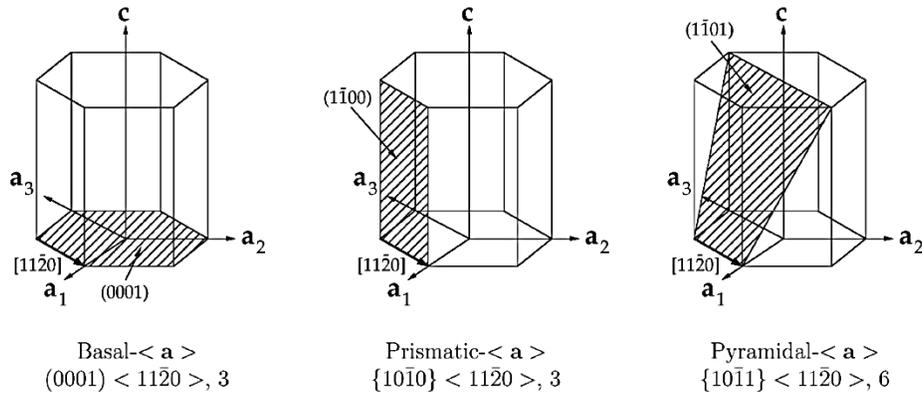
Figure 2.1 – Slip systems in hcp materials (Staroselsky and Anand, 2003).

The majority of previous research on magnesium sheet has been conducted on AZ31B. Lou *et al*. (2007) studied the deformation mechanisms of AZ31B in tension and compression at room temperature and observed that tensile deformation is initially dominated by basal slip with other contributions from non-basal slip as the flow stress increases. Other slip systems such as non-basal slip on prismatic or pyramidal planes have higher critical resolved shear stress (CRSS) and activate at higher applied stresses. In Lou *et al*. (2007), in-plane compression tests revealed that twinning was the dominant deformation mechanism. Similar observations have been reported by Starosesky and Anand (2003) for AZ31B rolled sheet. Contrary to basal slip that is believed to be temperature independent (Ulacia *et al*., 2010), the CRSS of non-basal slip systems decreases with increasing temperature which leads to the good elevated temperature ductility of magnesium alloys (Agnew and Dugulu, 2005). Uniaxial compression tests performed at elevated temperatures by Jian and Agnew (2007) and Piao *et al*. (2012) showed that initial yield points were insensitive to temperature; thus an athermal mechanism should be responsible for yielding in compression. Twinning is known to be athermal (Khan *et al*., 2011) and is the dominant mechanism for in-plane compression of AZ31B. Therefore, an increase in deformation temperature can improve the formability of magnesium alloys (Boba *et al*., 2017; Ghaffari Tari *et al*.; 2013). As shown by Boba *et al*., (2017), ZEK100 exhibits superior ductility compared to AZ31B in terms of forming limit diagrams (FLD). Also forming operations performed on AZ31B and ZEK100 at elevated temperatures by Malcolm *et al*. (2014) showed that only ZEK100 can be utilized for inner door panels of cars.

The significant anisotropy in magnesium sheet alloys stems from the strong crystallographic textures developed during the rolling processes. Comparing AZ31B and ZEK100, Kurukuri *et al*. (2014a) studied the pole figures of AZ31B rolled sheet and reported that the material exhibits a strong basal pole figure with a minor spreading in the rolling direction. This data indicates that the majority of the grains are oriented with their c-axes along the sheet normal direction, with some grains tilted towards the sheet rolling direction. However, addition of the RE elements can modify the texture (Imandoust *et al*., 2017). In ZEK100 the basal texture intensity is weakened with spreading of the c-axes along the transverse direction of the sheet which is typical of RE magnesium alloys (Sinclair and Martin, 2013). The peak intensity of pole figures in ZEK100 is about one-fourth of that of AZ31B that leads to improved formability; however, as argued by Habib *et al*. (2017) and Kurukuri *et al*. (2014b), a high orientation dependency persists which results in even stronger in-plane anisotropy. Constitutive plastic response of magnesium alloys will be further discussed in the next section.

2.2. Characterization of Plastic Response

In general, there are two major approaches to describe plasticity or yielding behaviour of polycrystalline materials. The first is the crystal plasticity approach which is based upon physical aspects of plastic deformation and on averaging the response over a large number of grains. The crystallographic texture is the main input for these models. Crystal plasticity models have been implemented into finite element codes and have successfully predicted the plastic response of materials (Inal *et al*., 2002; Plunkett *et al*., 2006; Grytten *et al*., 2008; Levesque *et al*., 2010; Rousselier and Luo, 2014; Qiao *et al*., 2015; 2017). Unfortunately, such finite element calculations are computationally expensive, thus limiting their applicability for industrial large-scale simulations. The second approach uses phenomenological continuum-based models to predict the yielding behaviour of materials. The computational times of phenomenological models are typically much faster than the crystal plasticity approach. In addition, they are easier to implement into finite element codes. These advantages lead to widespread usage of phenomenological models in industrial applications. This section is devoted to a brief description

of phenomenological plasticity models and flow rules employed in sheet metal forming and crash simulations for predicting plastic response of materials.

2.2.1. Phenomenological Yield Functions

Phenomenological isotropic yield functions such as Tresca or von Mises are among the oldest models still in use in industry and academia. Hershey (1954) and Hosford (1972) proposed non-quadratic isotropic yield functions to obtain better accuracy than the quadratic von Mises yield criterion. The yield function of Hosford (1972) is given by:

$$\Phi_{Hosford} = \left[\frac{1}{2} \left((\sigma_1 - \sigma_2)^a + (\sigma_1 - \sigma_3)^a + (\sigma_2 - \sigma_3)^a \right) \right]^{\frac{1}{a}} \tag{2.1}$$

where σ_{1-3} are the principal stresses and a is the exponent of the yield function. The Hosford yield criterion is appropriate for materials with a random crystal orientation distribution; however, most rolled sheet materials, in particular magnesium alloys, exhibit preferred (non-random) textures and require anisotropic yield functions.

One of the earliest phenomenological anisotropic yield functions was proposed by Hill (1948). This quadratic yield function, often referred to as the Hill48 model, resulted in acceptable predictions for traditional steels; however, with the advent of more advanced alloys and non-ferrous metals, it was experimentally observed that the Hill48 model is not capable of describing the yielding behaviour of these metals accurately, specifically under biaxial stress states (Aretz and Barlat, 2013). Later on, Hill proposed various anisotropic yield functions (*e.g.* Hill, 1979; 1990; 1993) to correct the shortcomings and anomalous responses of the Hill48 function. Nonetheless, the popularity of the Hill48 model still persists in industry and academia due to its simplicity and availability in most of the commercial finite element software codes (*e.g.* Chung *et al*., 2011; Mirone and Corralo, 2013; Park *et al*., 2017; Coer *et al*., 2017).

Perhaps the largest contributions to anisotropic phenomenological yield functions are found in the Barlat family of yield criteria (Barlat and Lian, 1989; Barlat *et al*., 1991; 1997; 2003; 2005; Aretz and Barlat, 2013). Following the isotropic yield function of Barlat and Richmond (1987),

Barlat and Lian (1989) proposed a plane-stress anisotropic yield function (so-called Yld89) based on a linear transformation of the stress deviator. The components of the transformation tensor are obtained from experiments under various loading conditions and in different material orientations. This methodology became the milestone for the rest of the Barlat family of anisotropy yield functions as isotropic yield functions are used as generators for the development of anisotropic yield functions. The purpose of the linear transformation operators is to put different weights to the components of the deviatoric stress while preserving convexity of the yield function. Following this procedure, the Yld91 model was proposed for 3-D stress states (Barlat *et al.*, 1991) followed by the Yld94 and Yld96 (Barlat *et al.*, 1997) to improve the accuracy of the yield functions. In 2003, the plane-stress Yld2000-2d model was proposed (Barlat *et al.*, 2003) which is currently a popular yield function for anisotropic modelling of sheet metals (*e.g.*, Yoon *et al.*, 2004; Andar *et al.*, 2012; Huh *et al.*, 2013; Athale *et al.*, 2017; Manopulo *et al.*, 2017). Subsequently, to account for 3-D formulations, Barlat *et al.* (2005) generalized the Yld2000-2d model to consider all six-components of the stress tensor which resulted in the Yld2004-18p yield criterion. The Yld2004-18p yield function of Barlat *et al.* (2005) is defined as:

$$\Phi_{Yld2004} = \left\{ \frac{1}{4}\left(\left|S_1' - S_1''\right|^a + \left|S_1' - S_2''\right|^a + \left|S_1' - S_3''\right|^a + \left|S_2' - S_1''\right|^a + \left|S_2' - S_2''\right|^a + \left|S_2' - S_3''\right|^a + \left|S_3' - S_1''\right|^a + \left|S_3' - S_2''\right|^a + \left|S_3' - S_3''\right|^a \right) \right\}^{1/a}$$

(2.2)

where S_{1-3}' and S_{1-3}'' are the principal values of transformed stress deviator $\boldsymbol{S'}$ and $\boldsymbol{S''}$, given by:

$$\boldsymbol{S'} = \boldsymbol{C'}:\boldsymbol{s} \ , \ \boldsymbol{S''} = \boldsymbol{C''}:\boldsymbol{s}$$

(2.3,2.4)

with the associated linear transformation tensors of:

$$\boldsymbol{C'} = \begin{bmatrix} 0 & -c_{12}' & -c_{13}' & 0 & 0 & 0 \\ -c_{21}' & 0 & -c_{23}' & 0 & 0 & 0 \\ -c_{31}' & -c_{32}' & 0 & 0 & 0 & 0 \\ 0 & 0 & 0 & -c_{44}' & 0 & 0 \\ 0 & 0 & 0 & 0 & -c_{55}' & 0 \\ 0 & 0 & 0 & 0 & 0 & -c_{66}' \end{bmatrix} \ , \ \boldsymbol{C''} = \begin{bmatrix} 0 & -c_{12}'' & -c_{13}'' & 0 & 0 & 0 \\ -c_{21}'' & 0 & -c_{23}'' & 0 & 0 & 0 \\ -c_{31}'' & -c_{32}'' & 0 & 0 & 0 & 0 \\ 0 & 0 & 0 & -c_{44}'' & 0 & 0 \\ 0 & 0 & 0 & 0 & -c_{55}'' & 0 \\ 0 & 0 & 0 & 0 & 0 & -c_{66}'' \end{bmatrix}$$

(2.5,2.6)

in Eqs. (2.3) and (2.4) *s* is the stress deviator. Note that the components of the $\boldsymbol{C'}$ and $\boldsymbol{C''}$ tensors are the anisotropy coefficients that should be calibrated with experimental data. The Yld2004-18p yield surface for an aluminum alloy (AA6111-T4) is shown in Figure 2.2. Although the Yld2004-18p model is computationally expensive and its calibration is not straightforward (Grytten *et al.*, 2008), it has been successfully used in simulation of forming and crashworthiness of aluminum alloys (Yoon *et al.*, 2006; Fourmeau *et al.*, 2011; 2013; Kohar *et al.*, 2017).
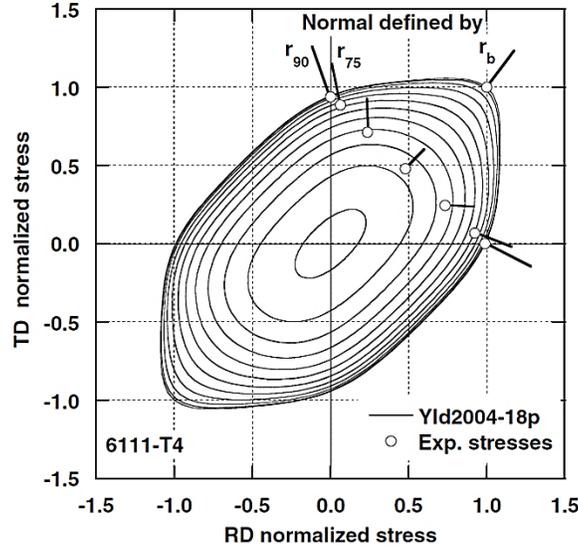
Figure 2.2 – Yield surface of AA6111-T4 represented with the Yld2004-18p formulation (Barlat *et al.*, 2005).

Based on the above literature review, very versatile anisotropic yield criteria exist in the literature; however, these models were intended for modelling bcc and fcc cubic materials. As described in the previous section, magnesium alloys have an hcp structure. In such materials the plastic deformation occurs by slip and twinning mechanisms, and, due to the directional sensitivity of the twining mechanisms, a strong tension-compression asymmetry is observed in the yield *loci* of these materials (Kurukuri *et al.*, 2014a,b; Habib *et al.*, 2017). To account for strength differential effects, Cazacu and Barlat (2004) generalized Drucker's isotropic yield criterion (Drucker, 1949) followed by an anisotropic extension developed by Cazacu *et al.* (2006) known as the CPB06 yield criterion based on the linear transformation approach. The CPB06 yield function is of the form:

$$\Phi_{CPB06} = \left(\left|\Sigma_1\right| - k\,\Sigma_1\right)^a + \left(\left|\Sigma_2\right| - k\,\Sigma_2\right)^a + \left(\left|\Sigma_3\right| - k\,\Sigma_3\right)^a \qquad (2.7)$$

where k is a constant that accounts for asymmetry. Also Σ_{1-3} are the principal values of the transformed stress deviator:

$$\Sigma = C : s \tag{2.8}$$

with the transformation tensor of:

$$C = \begin{bmatrix} C_{11} & C_{12} & C_{13} & 0 & 0 & 0 \\ C_{12} & C_{22} & C_{23} & 0 & 0 & 0 \\ C_{13} & C_{23} & C_{33} & 0 & 0 & 0 \\ 0 & 0 & 0 & C_{44} & 0 & 0 \\ 0 & 0 & 0 & 0 & C_{55} & 0 \\ 0 & 0 & 0 & 0 & 0 & C_{66} \end{bmatrix} \tag{2.9}$$

The components of the C tensor are the anisotropy coefficients that should be determined from experimental data. Later, Plunkett *et al.* (2008) demonstrated that the accuracy of the CPB06 model can be significantly improved if more than one linear transformation was applied on the stress deviator. A model with n-times of stress transformations, denoted as CPB06exn, can be written as:

$$\Phi_{CPB06exn} = \Phi_{CPB06}^{(1)} + \Phi_{CPB06}^{(2)} + \ldots + \Phi_{CPB06}^{(n)} \tag{2.10}$$

with each transformation tensor having its own independent coefficients:

$$\Sigma^{(i)} = C^{(i)} : s \quad , \quad C^{(i)} = \begin{bmatrix} C_{11}^{(i)} & C_{12}^{(i)} & C_{13}^{(i)} & 0 & 0 & 0 \\ C_{12}^{(i)} & C_{22}^{(i)} & C_{23}^{(i)} & 0 & 0 & 0 \\ C_{13}^{(i)} & C_{23}^{(i)} & C_{33}^{(i)} & 0 & 0 & 0 \\ 0 & 0 & 0 & C_{44}^{(i)} & 0 & 0 \\ 0 & 0 & 0 & 0 & C_{55}^{(i)} & 0 \\ 0 & 0 & 0 & 0 & 0 & C_{66}^{(i)} \end{bmatrix} \tag{2.11,2.12}$$

It should be noted that the number of the calibration parameters increases by the number of the stress transformations; thus more experimental data is required to calibrate anisotropic yield functions with multiple stress transformations. Figure 2.3 shows a schematic of the CPB06 yield loci for an anisotropic-asymmetric magnesium alloy. It can be seen that the shape of the yield *loci* do not remain constant and change with deformation reflecting the evolution of texture with deformation (Kurukuri *et al.*, 2014b).

9
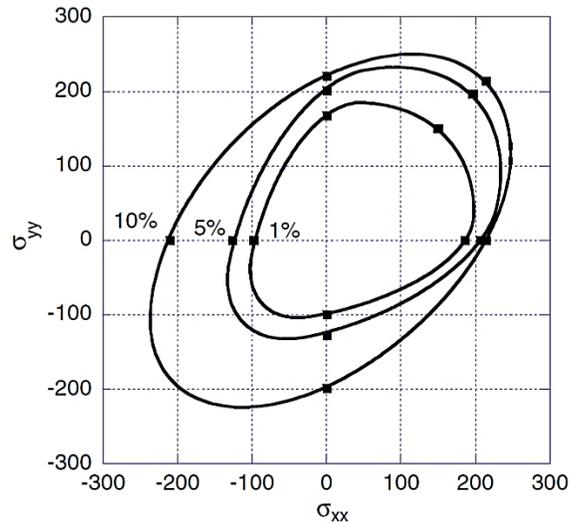
Figure 2.3 - Yield *locus* of Mg-0.5%Th sheet calibrated with the CPB06 model with one stress transformation at the three levels of plastic deformation (Cazacu *et al.*, 2006).

The CPB06 criterion has been successfully employed by several researchers for simulating the behaviour of hcp materials. Kim *et al.* (2008) used the CPB06 yield function to simulate three-point bending of AZ31B magnesium alloy sheet. A similar approach was adopted by Barros *et al.* (2016) for four-point bending of AZ31B and zirconium alloys. Moreover, Andar *et al.* (2012) used the CPB06 formulation with three transformations to evaluate the yield surface of AZ31B sheet. Simulations of spherical and elliptical bulge tests of an hcp titanium sheet were performed by Williams and Boyle (2016) using the CPB06 model. In terms of evolution of anisotropy with deformation, Ghaffari Tari *et al.* (2014) used the CPB06 model with one to four linear stress transformations to simulate the response of an AZ31B rolled sheet in which the components of transformation tensors were a function of deformation and evolved with plastic strain. More recently, Tuninetti *et al.* (2015) used the CPB06 model with a similar evolution technique for modelling tension-compression asymmetry of a titanium alloy. These computationally expensive models resulted in significant improvements in accuracy for modelling evolutionary anisotropic behaviour of hcp alloys.

2.2.2. Flow Rules

In addition to a yield function, a plasticity model requires an appropriate flow rule or plastic potential function to predict direction of plastic flow. For this purpose, available models in the literature are based on either the associative flow rule (AFR) or the non-associative flow rule (non-AFR). In the AFR, the yield function is also the plastic potential for calculating the plastic strain increments (see Figure 2.4). AFR models have been employed in the majority of the works published in the literature including the papers cited above. The classical work of Bishop and Hill (1951) demonstrated that the AFR holds for metals based on a crystal plasticity model. However, in the last decades, the assumption of the AFR has been challenged by the non-AFR in which the plastic potential is independent from the yield function (*e.g.* Stoughton, 2002; Cvitanic *et al*., 2008, see Figure 2.4). It is shown by Stoughton *et al*. (2002) that the difficulties encountered in simulations with the AFR Hill48 model in the biaxial region can be overcome by adopting the non-AFR. Considering materials with severe anisotropy, the non-AFR provides a higher degree of flexibility for calibrating yield stresses and r-values, a feature that can be utilized for magnesium alloys with complex anisotropy.

In terms of stability, Drucker (1949) showed that models based on the AFR are always stable provided that the yield function is convex; however, Stoughton and Yoon (2006) discussed that the AFR is not the only postulate for stability. These authors proved that by imposing the following constraint, the rate of change of stress and plastic strain are uniquely defined which is a necessary condition for stability:

$$\frac{\partial \bar{\sigma}}{\partial \varepsilon_{eq}^{p}}(\frac{\Psi}{\Phi}) + \frac{\partial \Phi}{\partial \boldsymbol{\sigma}} : \mathbf{L} : \frac{\partial \Psi}{\partial \boldsymbol{\sigma}} > 0 \tag{2.13}$$

where Ψ is the plastic potential, $\bar{\sigma}$ is the equivalent stress, and $\mathbf{L}$ is the stiffness tensor. There are other constraints that have been mentioned by Stoughton (2002) and Stoughton and Yoon (2006) for stability of non-AFR models; however, from the point of view of implementation of the model into finite element codes, the constraint of Eq. (2.13) is the most important (Safaei, 2013).

The Hill48 model with the non-AFR has been successfully employed for modelling plastic deformation of aluminum alloys (*e.g.* Stoughton and Yoon, 2009; Taherizadeh *et al*., 2010; Mohr

et al., 2010; Qian *et al.*, 2017). Similarly, due to the high flexibility of the non-AFR in capturing anisotropy in plastic flow, Park and Chung (2012), Safaei *et al.* (2013), and Hippke *et al.* (2017) used the non-AFR Yld2000-2d criterion to simulate earing profiles of aluminum sheets in cup drawing tests. More recently, Noder (2017) successfully simulated formations of eight ears in cup drawing tests of 7000-series aluminum alloy sheet. It is worth mentioning that, concerning evolution of anisotropy for materials such as magnesium alloys, models with the non-AFR enable the possibility that plastic potential and yield function evolve differently, a feature that is not possible in models based on the AFR. Despite these apparent advantages, plasticity models with the non-AFR have not been evaluated for magnesium alloys, the one exception being a recent work by Zhang *et al.* (2017) who used a pressure dependent yield function and the Hill48 plastic potential for AZ31B.
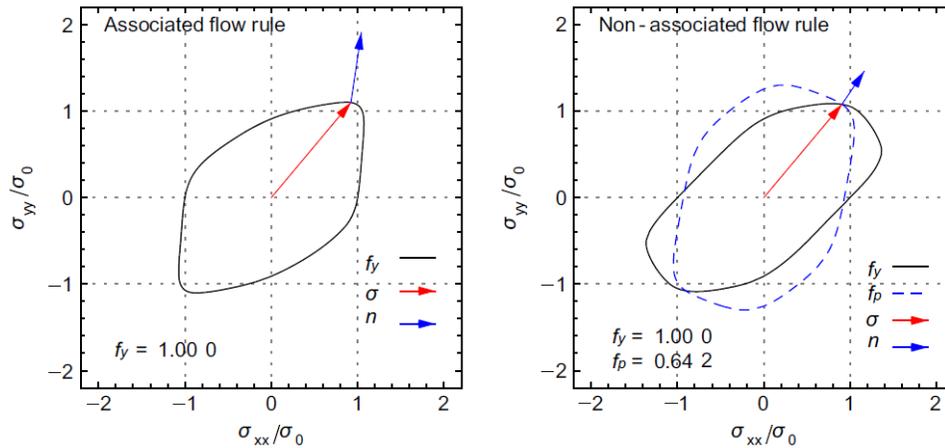
Figure 2.4 – Concepts of associative (left) and non-associative (right) flow rules (Safaei *et al.*, 2013). f_y is the yield function and f_p is the plastic potential.

2.3. Ductile Fracture

The prediction of ductile fracture in sheet metals is a crucial topic in forming and crashworthiness applications. The present section deals with introducing different modelling approaches to predict ductile fracture of un-cracked bodies. The models that are presented herein are used to predict the initiation of cracks in initially intact materials undergoing different loading conditions. These models are usually categorized into: micromechanical, continuum damage mechanics, and phenomenological models.

2.3.1. Micromechanical Approaches

Microscopically, ductile fracture is induced by the nucleation, growth, and coalescence of voids which ultimately form a visible macroscopic crack. These three stages are shown schematically in Figure 2.5. The role of micro-voids in ductile fracture was first studied by McClintock (1968). In this study, the evolution of an isolated cylindrical void in a ductile elastoplastic matrix was analyzed. Rice and Tracey (1969) investigated the evolution of spherical voids in an elastic-perfectly plastic matrix. In these papers, the interaction between micro-voids, the coalescence process, and hardening effects were neglected and fracture was assumed to occur when the void volume fraction reaches a critical value specific for each material. Hancock and Mackenzie (1976) indicated that ductility of materials depends markedly on the stress triaxiality. They reported that coalescence of two adjacent voids in high strength steels is accommodated by generation of a large number of secondary smaller voids. These studies showed that the rate of void growth is controlled by the stress triaxiality; therefore, hydrostatic pressure is a critical factor in damage modelling.

The concept of a shrinking yield surface due to the combined effects of damage and hydrostatic pressure was put forward by Gurson (1977). He studied a finite sphere containing an isolated spherical void in a rigid perfectly plastic matrix and employed the void volume fraction as an internal variable to represent damage and its softening effect on material strength. The original Gurson model has been repeatedly modified to account for additional factors responsible for material deterioration and subsequent fracture, such as: void nucleation (*e.g.* Chu and Needleman, 1980), void coalescence (*e.g.* Tvergaard and Needleman, 1984), and void shape effects (*e.g.* Gologanu *et al*., 1993, 1994; Pardoen and Hutchinson, 2000). The Gurson model modified by Tvergaard and Needleman (1984) is usually referred to as the GTN model.
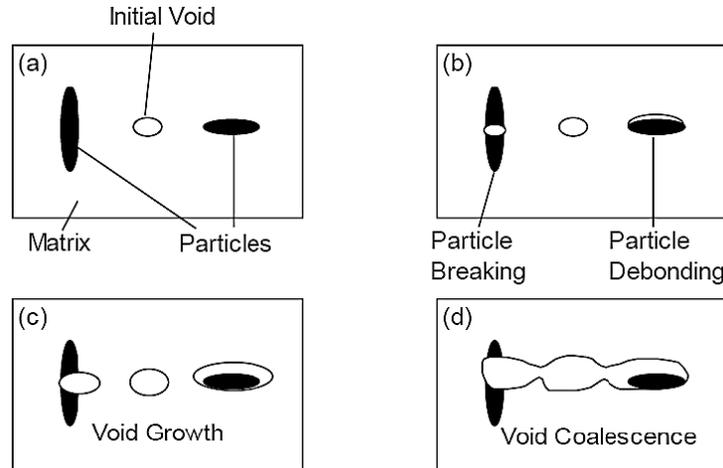
Figure 2.5 – Damage evolution: (a) initial state, (b) void nucleation, (c) void growth, and (d) void coalescence (Chen, 2004).

The GTN model can be used to predict the softening and damage of materials in which the void damage mechanism plays the dominant role. However, in ductile solids undergoing shear-dominated deformation with low stress triaxiality, the damage behaviour is very different from that observed at higher triaxiality levels. For example, under shear dominated loading conditions, significant void growth is usually not observed whereas distortion of voids and inter-void linking play a critical role in material degradation (Brunig *et al*., 2013). These mechanisms are not predicted by the GTN model; consequently, traditional GTN models are unable to predict fracture under shear dominated loading conditions. Nahshon and Xue (2009) and Nielsen and Tvergaard (2010) modified the original Gurson model to correct the fracture prediction under shear loading conditions. In these shear-modified GTN models, the micromechanical justifications of the models are lost due to empirical assumptions made to model the effect of the shear loading conditions (Dunand and Mohr, 2011; Ghahremaninezhad and Ravi-Chandar, 2013). Note that another shortcoming of the GTN damage model is the calibration procedure in which a large number of coupled parameters have to be determined for a single material.

It should be noted that the ductile fracture mechanisms described above might not be valid for magnesium alloys. Abedini *et al*. (2015) examined microstructure of fracture surfaces of ZEK100 alloy using scanning electron microscope (SEM) in which the micrographs of shear specimens showed smooth surfaces (Figure 2.6 a,b) while the surface of the tensile specimen in

14

Figure 2.6c exhibited a typical dimpled surface. However, recent microstructural investigations of fracture in magnesium alloys conducted by Ray and Wilkinson (2016) and Nemcko and Wilkinson (2016) revealed the role of grain boundaries and twin boundaries on fracture initiation sites. Unlike conventional steel and aluminum alloys, it was observed that void nucleation rarely occurs from second phase particles or inclusions in microstructure of magnesium.
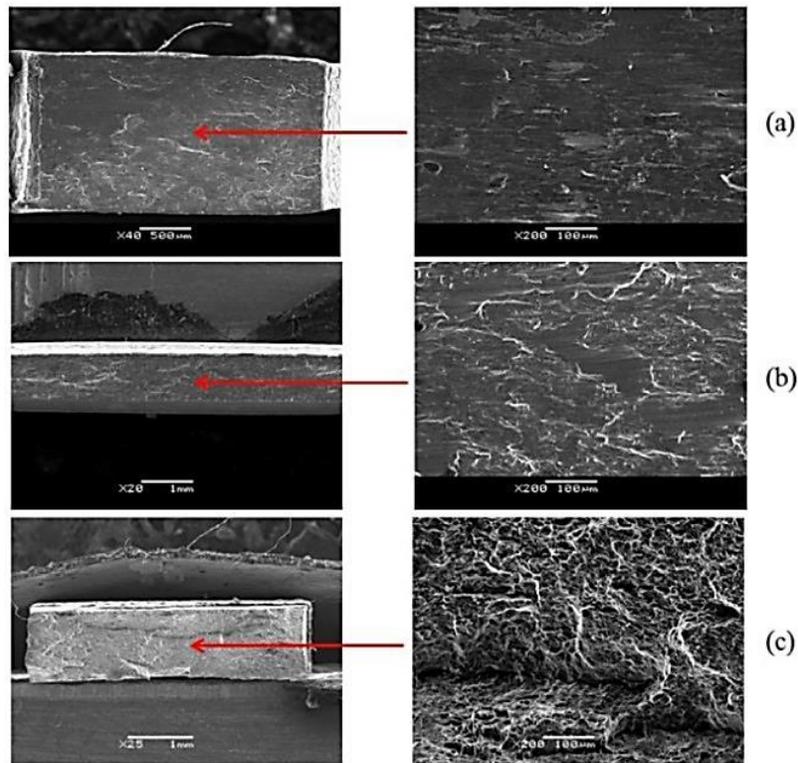
Figure 2.6 – SEM images of the fracture surfaces of (a, b) shear and (c) uniaxial tensile specimens of ZEK100 (Abedini *et al*., 2015).

2.3.2. Continuum Damage Mechanics Approaches

An alternative approach for fracture prediction is continuum damage models (CDM). The CDM models were first introduced by Kachanov (1958) in the study of creep problems while Lemaitre (1985) was the first to use the CDM approach for modelling ductile fracture. In this method, the details of nucleation, growth, and coalescence of voids are ignored and the deterioration of the material is described by a damage variable which is defined as an internal state variable. Also in this method, a thermodynamics dissipation potential is introduced to obtain the damage evolution law in a continuous media (Lemaitre, 1985). In the CDM approach,

the measure of the damage amplitude in a given plane is obtained by measuring the area of intersection of all defects with that plane. For instance, based on Figure 2.7, it is readily observed that the effective area of the sample is S-S_D, where S is the total area and S_D represents the damaged (void) area in the considered plane. The effective area withstands the load and in the absence of damage, the effective area is equal to the initial area. The positive scalar $\overline{D}$ is considered as a damage variable and is expressed by:

$$\overline{D} = \frac{S_D}{S}$$
(2.14)

For a uniaxial loading with an applied load of F, based on the principle of strain equivalence, the effective stress ($\tilde{\sigma}$) is defined by:

$$\tilde{\sigma} = \frac{F}{S - S_D}$$
(2.15)

which means that for the same value of strain, the damaged material experiences higher stress than that of the undamaged material. In order to consider the evolution of the damage, a dissipation potential with its evolution rules is adopted from constitutive rules of thermodynamics (Allahverdizadeh *et al*., 2012). Compared to the micromechanical models, the CDM models are formulated in a phenomenological manner with a thermodynamics framework and fewer material constants for calibrations (Tutyshkin *et al*., 2014).
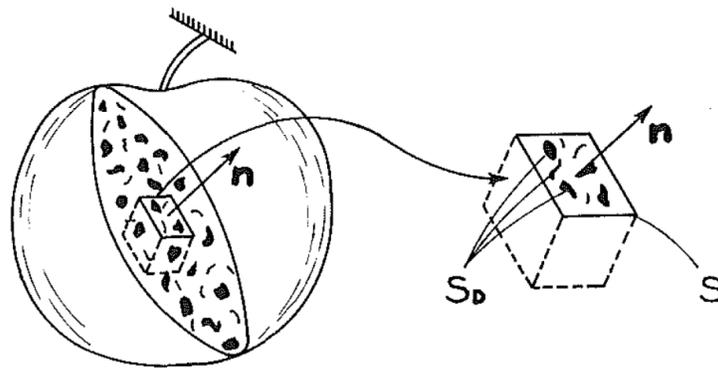
Figure 2.7 – Schematic of a damaged element (Lemaitre, 1985).

2.3.3. Phenomenological Approaches

The damage models described above are also known as coupled damage models in which the constitutive plasticity and fracture models are coupled. Alternatively, uncoupled fracture models consider fracture as a sudden event when the stress and strain states of an undamaged material reach a critical level. Uncoupled phenomenological fracture models have been developed by neglecting the effect of damage on the plastic behaviour of materials prior to fracture; therefore, one can utilize any desired metal plasticity model together with a separate phenomenological fracture model. No assumptions are made upon the physical fracture mechanisms. From an industrial point of view, a good damage model should be easily calibrated from physical tests and efficiently implemented into finite element codes. Micromechanical and CDM damage models do not meet these requirements; therefore, phenomenological models are more popular in industrial applications.

In terms of the stress state dependency, most of the early phenomenological models were only a function of the stress triaxiality (*e.g.* Oyane *et al*., 1980; Clift *et al*., 1990). More recent studies have demonstrated the importance of the Lode parameter in addition to the stress triaxiality in predicting ductile fracture (Bao and Wierzbicki, 2004; Bai and Wierzbicki, 2008, 2010; Mohr and Marcadet, 2015). These models lead to a construction of fracture surfaces in the 3-D space of stress triaxiality, Lode parameter, and equivalent strain at fracture strain, ε_f :

$$\varepsilon_f = f(\eta, \bar{\theta}) \tag{2.16}$$

$$\eta = -\frac{\sigma_{hyd}}{\sqrt{3J_2}} \quad , \quad \theta = \frac{1}{3}\cos^{-1}(\frac{3\sqrt{3}}{2}\frac{J_3}{J_2^{\frac{3}{2}}}) \quad , \quad \bar{\theta} = 1 - \frac{6\theta}{\pi} \tag{2.17-2.19}$$

where σ_{hyd} is the hydrostatic stress, and J_2 and J_3 are the second and third invariants of the stress deviator. Also η is the stress triaxiality and $\bar{\theta}$ is the Lode parameter.

Inspired by the micromechanical model of Rice and Tracy (1969), Bai and Wierzbicki (2008) assumed that the relationship between the fracture strain and triaxiality is in exponential form and they assumed a parabolic form to represent the influence of the Lode parameter. Hence the following form of the fracture *locus* was postulated:

$$\varepsilon_f(\eta,\bar{\theta}) = \left[\frac{1}{2}(D_1 e^{-D_2\eta} + D_5 e^{-D_6\eta}) - D_3 e^{-D_4\eta}\right]\bar{\theta}^2 + \frac{1}{2}(D_1 e^{-D_2\eta} - D_5 e^{-D_6\eta})\,\bar{\theta} + D_3 e^{-D_4\eta} \qquad (2.20)$$

In this fracture *locus* function, six parameters of D_{1-6} need to be calibrated from experimental tests. Figure 2.8 shows a 3-D fracture surface for an aluminum alloy obtained from this model.
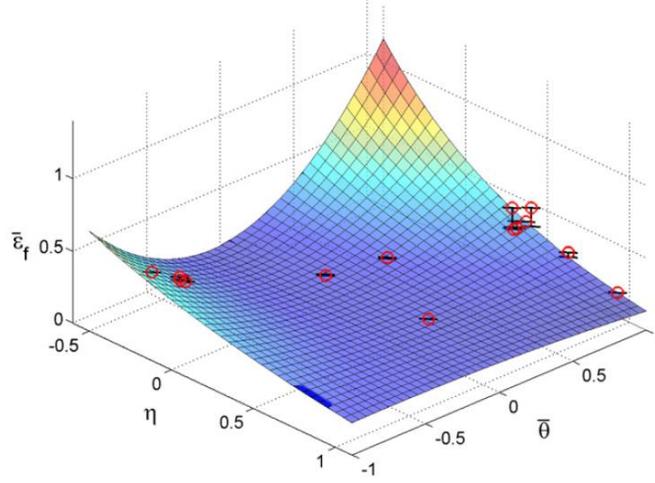
Figure 2.8 – Fracture *locus* of AA2024-T351 in the space of fracture strain, stress triaxiality, and Lode parameter (Bai and Wierzbicki 2008). The symbols show experimental data.

It is worth mentioning that the shape of the locus of fracture strain versus stress triaxiality is a topic of debate. The phenomenological models described above commonly lead to a non-monotonic fracture curve as shown in Figure 2.9(a) (blue curve). However, the experimental data of Haltom *et al.* (2013) and Ghahremaninezhad and Ravi-Chandar (2013) exhibited a monotonic trend (Figure 2.9b). It should be noted that the choice of gauge length is critical for shear loading and local shear strains measured microscopically near the fracture surface resolved from grain rotations can be much higher than the strains reported from DIC measurements that average the strains over a larger area (Rahmaan *et al.*, 2017).
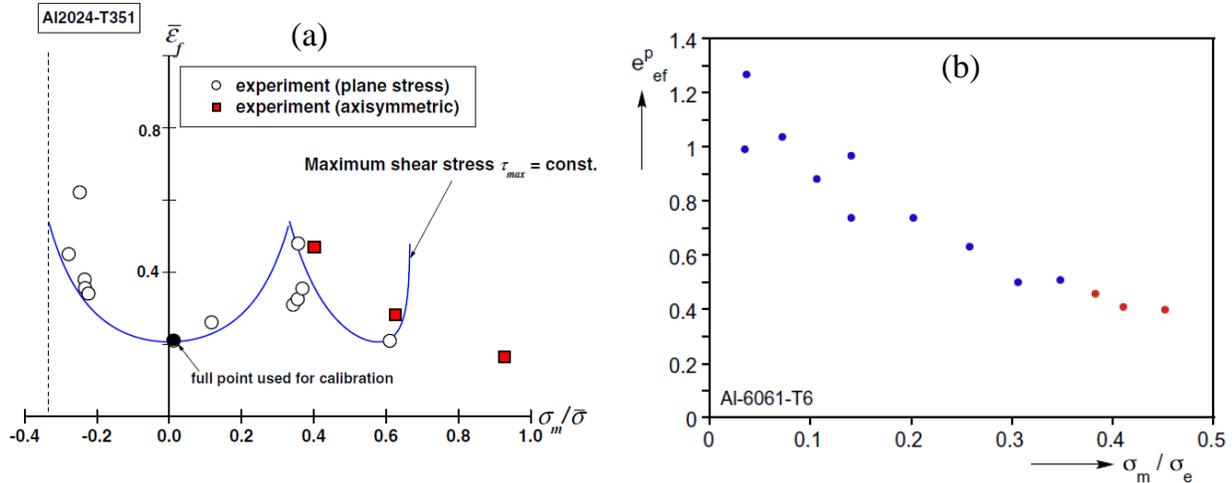
Figure 2.9 – Fracture strain versus stress triaxiality for (a) AA2024-T351 from Bai and Wierzbicki (2010) and (b) AA6061-T6 from Haltom *et al*. (2013).

The fracture models introduced above were proposed for isotropic materials and not applicable for anisotropic materials. However, these models have been modified in the literature to consider fracture of anisotropic materials. For instance, Luo *et al*. (2012) used the idea of linear transformation of the stress tensor commonly employed in developing anisotropic yield functions, to transform the plastic strain tensor and account for anisotropy in fracture strains within the phenomenological framework. Similar approaches were also used by Jia and Bai (2016) and Lou and Yoon (2017) for ductile fracture modelling of AZ31B magnesium and 6000 series aluminum alloys, respectively.

2.3.4. Damage under Proportional and Non-proportional Loading

Proportional loading condition is defined when the stress state remains constant during deformation. While achieving proportional loading is often desired for characterization of materials, understanding the behaviour of materials under non-proportional conditions is essential since in forming operations and in crash events, materials are subjected to complex stress state changes. Moreover, non-proportionalities commonly arise due to the structural response of materials such as bucking or plastic instability. The role of the non-proportional loading conditions on the yielding behaviour of materials is well-established with concepts of the kinematic hardening (Chaboche, 2008) and distortional hardening in homogeneous anisotropic

19

hardening (HAH) models (Barlat *et al.*, 2011; 2017). As opposed to the published research on the role of non-proportionality on yielding response, there exist limited studies on fracture characterization of materials under non-proportional conditions.

Bao and Treitler (2004) performed notch compression tests on axisymmetric AA2024-T351 bars followed by tension tests to fracture in which a substantial increase in ductility was reported due to the pre-straining in compression. Basu and Benzerga (2015) studied a conventional medium-carbon steel alloy by uniaxial tension with axisymmetric bars followed by machining notches on the specimen to increase the stress triaxiality. Moreover, the influence of the loading direction reversal on the onset of fracture of DP780 steel sheet was investigated by Marcadet and Mohr (2015) through compression-tension experiments (Figure 2.10) and it was reported that the strain to fracture was increased by pre-straining in compression. A similar study was also performed by Papasidero *et al.* (2015) on AA2024-T351 tubes by pre-straining the material in tension, compression, and torsion in which it was observed that applying pre-compression and pre-torsion increased the ductility while applying pre-tension reduced the ductility of the material. More recently, ten Kortenaar (2016) studied the influence of non-proportional loadings on fracture behaviour of a boron steel sheet under different loading conditions after imposing an initial biaxial pre-straining (Figure 2.11).
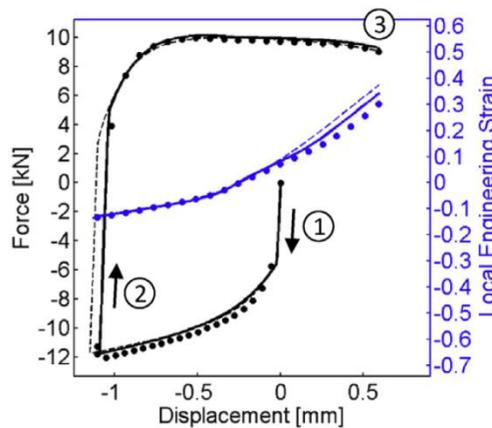
Figure 2.10 – Non-proportional tests of (1) uniaxial compression (2) followed by unloading (3) and subsequent tension on a DP780 steel sheet (Marcadet and Mohr, 2015). Note that the symbols show the experimental data and the curves represent the results of a model described by Marcadet and Mohr (2015).
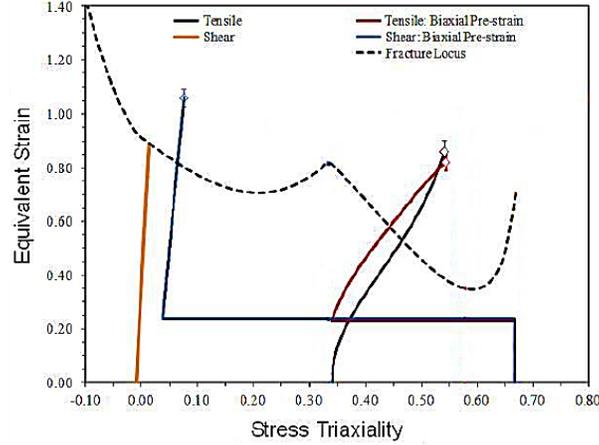
Figure 2.11 – Fracture strain *versus* triaxiality of a boron steel sheet after biaxial pre-straining (ten Kortenaar, 2016).

Uncoupled phenomenological models employ a damage parameter to predict material fracture. This variable is often taken as a weighted cumulative plastic strain, in which the weighting function accounts for the effect of the stress state on the fracture initiation. When the damage parameter reaches a critical value, the phenomenological models predict the onset of fracture. The damage parameter, *D*, can be written as:

$$D = \left[\frac{\varepsilon_{eq}^p}{\varepsilon^f(\eta,\overline{\overline{\theta}})} \right]^m \tag{2.21}$$

where ε_{eq}^p is the equivalent plastic strain and *m* is the damage exponent. It is important to emphasize that the formulation in Eq. (2.21) is purely phenomenological and only strictly valid for proportional loading conditions. For the case of non-constant stress triaxiality and Lode parameter, Eq. (2.21) can be written in the incremental form, such that the cumulative *D* can be obtained with the following integration:

$$D = \int \frac{m}{\varepsilon^f(\eta,\overline{\overline{\theta}})} \left[\frac{\varepsilon_{eq}^p}{\varepsilon^f(\eta,\overline{\overline{\theta}})} \right]^{m-1} d\varepsilon_{eq}^p \tag{2.22}$$

For the case of a linear damage accumulation with *m*=1.0, Eq. (2.22) reduces to:

$$D = \int \frac{d\varepsilon_{eq}^p}{\varepsilon^f(\eta,\overline{\overline{\theta}})} \tag{2.23}$$

21

Eqs. (2.21-2.23) suggest that damage starts to accumulate from the onset of plastic deformation up to fracture when the damage parameter D reaches unity. As shown in Figure 2.12, the rate of increasing D is determined by the exponent m in which slow ($m>1.0$) to fast ($m<1.0$) rates of damage with respect to plastic deformation can be obtained, and $m=1.0$ results in a linear damage accumulation. Despite the importance of considering non-proportional loading conditions, to the author's knowledge, there have not been any studies on fracture of magnesium alloys under severe changes of stress state to assess the approach of Eqs. (2.21-2.23) in treating damage under non-proportional conditions.
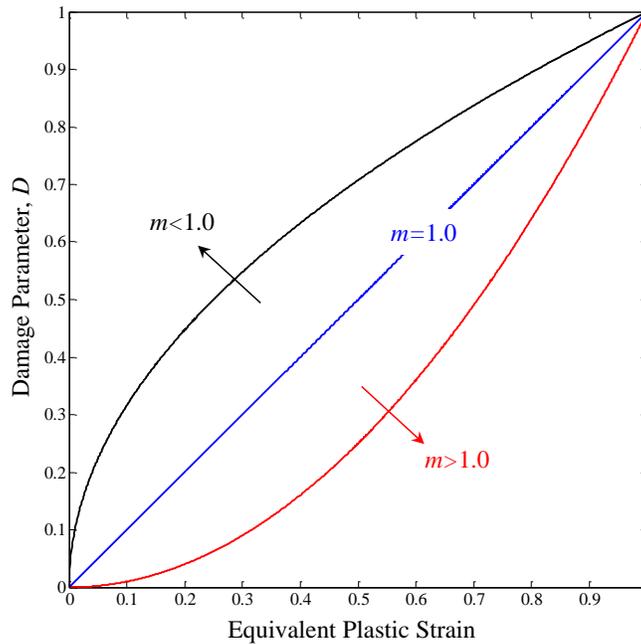
Figure 2.12 – Accumulation of the damage parameter, D, with plastic deformation for different ranges of the damage exponent.

2.4. Summary and Current Deficits in the Literature

Magnesium alloy sheets have attracted considerable attention because of their high strength-to-weight ratio; however, due to poor ductility at room temperature, they currently have limited commercial applications. The low ductility is mainly related to the limited number of available deformation mechanisms in the hcp microstructure of magnesium alloys, while the asymmetry/anisotropy results from the directional sensitivity of twinning mechanisms and the strong crystallographic textures imposed during manufacturing processes. The addition of RE

elements to magnesium alloys has been reported to modify the texture leading to improved ductility.

The anisotropic constitutive response of materials with strong textures has been extensively studied in the literature through crystal plasticity and phenomenological approaches. The phenomenological models are mainly based on single or multiple linear transformations of the stress deviator and have been successfully applied to alloys with cubic and hcp crystallographic structures. Although this approach has been used for several hcp materials, such as AZ31B magnesium and titanium alloys, the literature review presented herein has not found studies for ZEK100-O magnesium alloy considering comprehensive investigations of appropriate yield functions used for modelling plasticity under a wide range of stress states. Furthermore, it was discussed that models based on the non-AFR provide some unique features that can be utilized to simulate the complex evolving anisotropic behaviour of magnesium alloys. Despite these benefits, plasticity models with the non-AFR have not been thoroughly evaluated for hcp alloys. Thus, there exists a need for modelling the plastic behaviour of magnesium alloys, capturing tension-compression asymmetry and their evolution. This is particularly the case of rare-earth magnesium alloys, despite their improved formability relative to the current AZ31B commercial alloy.

Micromechanical, CDM, and phenomenological approaches are used in the literature to characterize damage in ductile materials. While the first two approaches are coupled with the plastic constitutive model, phenomenological models are uncoupled from plasticity. The topic of the phenomenological fracture modelling of metals displaying fracture anisotropy has been barely touched in the literature; specifically, there are no research investigations in which the ductility of highly anisotropic RE magnesium sheets is addressed. The fracture response of ZEK100-O has not been studied in the literature under proportional loading conditions. Moreover, the fracture behaviour of magnesium alloys under non-proportional loading has not been investigated. Clearly, the fracture behaviour of rare-earth magnesium alloys, such as ZEK100-O requires further attention.

3. Objectives

The overall aim of this research project is to enhance understanding of the constitutive and fracture behaviour of anisotropic sheet materials exhibiting complex anisotropic and asymmetric yielding. To this end, an experimental effort to characterize the room temperature anisotropic constitutive plasticity and fracture response has been performed considering ZEK100-O magnesium alloy sheet. This material was selected since it exhibits strong evolving anisotropic and complex tension-compression asymmetric response and has potential for industrial application within light-weight automotive body panels. Constitutive models are developed to capture evolving anisotropy and tension-compression asymmetry and an assessment of current fracture methodology is undertaken for this material. Based on the current research needs identified in the preceding literature review, the primary objectives for this thesis are defined as follows:

1. Characterize the constitutive plastic behaviour of ZEK100-O at room temperature, under quasi-static conditions for a range of proportional loading states;
2. Develop a phenomenological plasticity model capturing the effects of evolving anisotropy and tension-compression asymmetry;
3. Characterize the fracture response of ZEK100-O at room temperature, under quasi-static conditions under proportional and non-proportional loading conditions;
4. Calibrate a phenomenological fracture model to assess the degree of anisotropy in fracture behaviour of the material;

Besides the experimental characterization tasks concerning the first and third objectives outlined above, the main goal of this work is the development of a material model applicable for finite element simulation of materials exhibiting complex evolving anisotropy and tension-compression asymmetry. The proposed model will be implemented into the finite element code, LS-DYNA, which is commonly used in academia and industry to simulate metal forming and crash events. The finite element model will be able to predict the evolving anisotropy of the material with the aid of an advanced plasticity model which is not currently available in commercial finite element codes as built-in models. The model will be applied to simulate the characterization experiments as a form of validation/assessment of global and local stress and strain fields.

4. Results

This thesis is organized into several parts. Within this synopsis, an overview of the main research results and key findings is provided. More detail concerning the experimental methodology, modelling approach, and results is provided in Appendices A-D each of which is a distinct peer-reviewed article, either published or submitted for publication in international journals:

Appendix A   Abedini A, Butcher C, Nemcko M J, Kurukuri S, Worswick M J, Constitutive characterization of a rare-earth magnesium alloy sheet (ZEK100-O) in shear loading: studies of anisotropy and rate sensitivity, *International Journal of Mechanical Sciences*, 2017, **128-129**:54-69.

Appendix B   Abedini A, Butcher C, Worswick M J, An evolving non-associative anisotropic-asymmetric plasticity model for magnesium alloys, *Submitted for possible publication*, 2017.

Appendix C   Abedini A, Butcher C, Worswick M J, Fracture characterization of rolled sheet alloys in shear loading: Studies of specimen geometries, anisotropy, and rate sensitivity, *Experimental Mechanics*, 2017, **57**:75-88.

Appendix D   Abedini A, Butcher C, Worswick M J, Experimental fracture characterization of an anisotropic magnesium alloy sheet in proportional and non-proportional loading conditions, *Submitted for possible publication*, 2017.

A number of tasks were undertaken in support of attaining the objectives defined for this research project. For the first objective, a large experimental campaign was required to reveal the plastic response of ZEK100-O sheet under different loading conditions with the applied loading along various orientations of the sheet. Detailed mechanical characterization tests of the subject material were conducted in tensile, compressive, and shear states to analyze the anisotropic-asymmetric yielding and hardening behaviour of the material. The characterization experiments were performed at room temperature, under quasi-static conditions. The results of these experiments will serve to calibrate and validate material models in the subsequent steps of the

work described below. This work is summarized in Section 4.1, with additional detail provided in Appendix A.

The comprehensive characterization work performed in the previous task was critical to focus the material model development effort, establishing an understanding of the behaviour of the material under a range of stress states commonly observed in sheet metal forming operations and crash events. Consequently, an evolving anisotropic-asymmetric material model was developed along with a non-associative flow rule in Appendix B to simulate the response of the material under different loading conditions. Section 4.2 briefly describes the development of the material model which is shown to be capable of capturing the complex behaviour of the material along with validations of the model through single-element simulations. Furthermore, to assess predictive capabilities of the model, full-scale simulations of coupon-level formability tests were performed and compared with experimental results in terms of global load-displacement as well as local strain fields, as summarized in Section 4.2 with additional detail provided in Appendix B.

In addition, a large number of experiments were performed to obtain the fracture behaviour of ZEK100-O, under various stress states with the results serving to achieve the third and fourth objectives of the research. In a similar manner to the plastic characterization tests, fracture tests were performed in different orientations with respect to the rolling direction of the sheet to reveal the anisotropic fracture behaviour of the material. Due to the importance of the shear state, Appendix C provides detailed experimental methodologies to obtain the response of the material under this state of stress while Appendix D supplies an overview of the fracture behaviour of the material over a wide range of stress states under proportional and non-proportional loading conditions. A synopsis of the key outcomes of Appendices C and D are given in Section 4.3.

The present research was focused on magnesium alloys to develop the methodology for characterization of plasticity and fracture. However, due to the complexities associated with magnesium, other alloys were also considered along with the magnesium to provide a contrast and to help evaluate the methods (with the papers listed in Appendix E). Specifically, a calibration constraint was proposed by Abedini *et al*., (2017b) for shear regions of plastic potential function and the constraint have been employed to develop the plasticity model in Appendix D as summarized in Section 4.2.

4.1. Constitutive Plastic Characterization

As described in Section 2.2.1, a significant anisotropy is commonly observed in plastic response of commercial sheets. To reveal these characteristic features, a comprehensive experimental program is required, and the goal of the present section is to describe these experiments and analyze their outcomes concerning the constitutive plastic response of a magnesium alloy sheet, ZEK100-O.

4.1.1. Material

The chemical composition of the 1.55 mm ZEK100-O rolled sheet is presented in Table 4.1. Neodymium (Nd) is the rare-earth element of the alloy that is known to randomize the texture and improve its formability. X-ray diffraction (XRD) analysis was performed and, as shown in Figure 4.1, the texture of ZEK100-O exhibits a spread of the basal poles along the transverse direction which is typical of rare-earth magnesium rolled sheets. It has been reported in the literature that the main role of the rare-earth addition is to randomize the texture (Imandoust *et al.*, 2017) by spreading the c-axes along the transverse direction. Thus, compared to AZ31B, ZEK100-O possesses a relatively weaker basal texture that translates to higher ductility; however, the in-plane anisotropy is stronger due to differences in the texture along the transverse versus rolling directions (Kurukuri *et al.*, 2014a; Habib *et al.*, 2017). It is discussed by Kurukuri *et al.* (2014b) that peak intensity of the pole figure of ZEK100 is about one-fourth of AZ31B that leads to superior ductility of ZEK100 compared to AZ31B.

Table 4.1 – Chemical composition of ZEK100-O.

Chemical Composition	Zn	Nd	Zr	Mn	Mg
(%wt)	1.3	0.2	0.25	0.01	balance
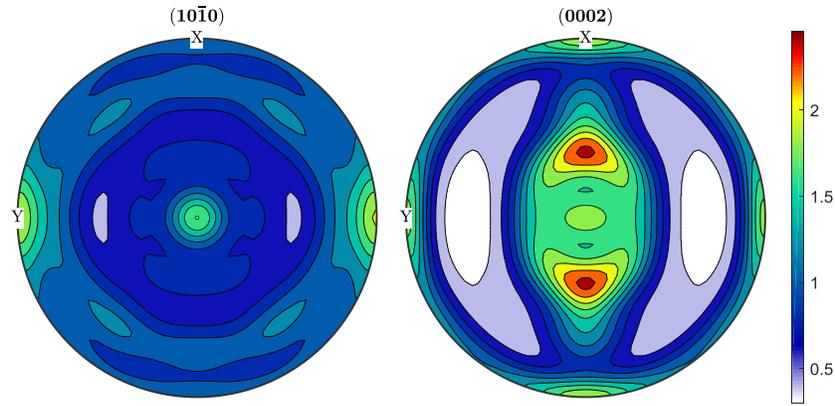
Figure 4.1 – XRD pole figures of the as-received ZEK100-O sheet. X and Y axes refer to the transverse and rolling directions, respectively.

4.1.2. Experiments and Methodology

The response of the material under different stress states was investigated at room temperature under quasi-static conditions (equivalent von Mises strain rate of approximately 0.001 s^{-1}). Uniaxial tensile tests were conducted using sub-sized ASTM E8 specimen shown in Figure 4.2(a) with samples extracted from the rolling direction (RD or 0°) to the transverse direction (TD or 90°) of the sheet in 15° increments (*i.e.* 0°, 15°, 30°, 45°, 60°, 75°, 90°). Furthermore, the experimental methodology of Kurukuri *et al*. (2014a,b) and Steglich *et al*. (2014) was followed for compressive states in which the adhesively bonded sample shown in Figure 4.2(b) was utilized. The compression tests were performed in the three directions of the RD, DD (45°), and TD with a custom-made compression device (see Appendix A for more detail). In addition, the same specimen geometry as in Figure 4.2(b) was employed to apply through-thickness compression loading to characterize the behaviour of the material under the equal-biaxial tensile stress state. Note that as discussed by Steglich *et al*. (2014), the through-thickness compression and equal-biaxial tensile states result in same deviatoric stress tensors and most yield functions assume that plastic yielding is independent from the hydrostatic stress, thus the through-thickness compression test can be employed as an alternative to the more complicated cruciform or bulge tests.

The shear response of the material was studied using a specimen type adopted from Peirs *et al*. (2012) with the geometry depicted in Figure 4.2(c). Shear samples were fabricated from the sheet to apply loading in the 45°, 90°, and 135° directions with respect to the rolling direction of

the sheet. The choice of the test orientations for shear tests is further discussed in Section 4.1.3 and in detail in Appendix A. The experiments described above were recorded using two digital cameras to obtain stereoscopic full-field logarithmic strains measurements using digital image correlation (DIC) techniques. To ensure repeatability of the experimental results, at least four specimens were tested for each specimen geometry and orientation. The tensile and shear experiments were performed using an MTS Criterion Model 45 servo-electric tensile frame while the compression tests were conducted with the custom-made compression rig installed on an Instron model 1331 servo-hydraulic tensile frame. More detail concerning the experimental methodology, specimen preparations, and extracting stress and strain data can be found in Appendix A.
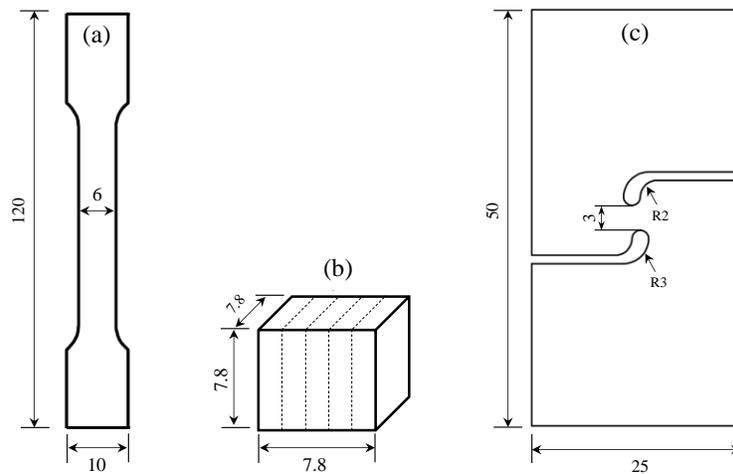
Figure 4.2 – Specimen geometries of (a) sub-sized ASTM E8, (b) stacked compression, and (c) shear. All dimensions are in millimetres.

4.1.3. Overview of Results

The constitutive plastic behaviour of the material under different loading conditions is shown in Figure 4.3. Note that the tensile data in Figure 4.3 is depicted up to the onset of necking, compressive results are shown up to the onset of delamination of specimens, and shear data is shown until fracture. It is apparent from Figures 4.3(a-c) that ZEK100-O displays a tension-compression asymmetric response which is due to the twinning mechanisms that are more dominant under the compression mode (Kurukuri *et al*., 2014a,b). Moreover, the evolving tensile r-values in Figure 4.3(d) highlight the evolution of the texture with deformation. Note that the

tensile response is only shown in three directions (RD, DD, and TD) in Figure 4.3 for brevity. The response of the material under the equal-biaxial tension state is shown in Figure 4.3(e) in which the uniaxial tensile response in the RD and TD orientations is also depicted for comparison. It can be seen that the equal-biaxial response of the material lies between that of the uniaxial tensile states. In addition, Figure 4.3(f) presents the behaviour of the material undergoing shear deformation in which anisotropy is apparent for initial yielding and hardening rates. The hardening response of the sample in 135° in Figure 4.3(f) exhibits a sigmoidal extension twinning signature which was confirmed by electron backscattered diffraction (EBSD) analysis of the microstructure of deformed specimens as described in Appendix A. It is worth mentioning that, as shown in Figure 4.4 for a shear test in the 135° orientation, the relationship between displacement and shear strain is not linear. In order to better observe the degree of anisotropy, uniaxial responses are compared in Figure 4.5 in terms of tensile (Figure 4.5a) and compressive (Figure 4.5b) behaviour. It is clear that the hardening rates and initial yield stresses show significant orientation dependency.
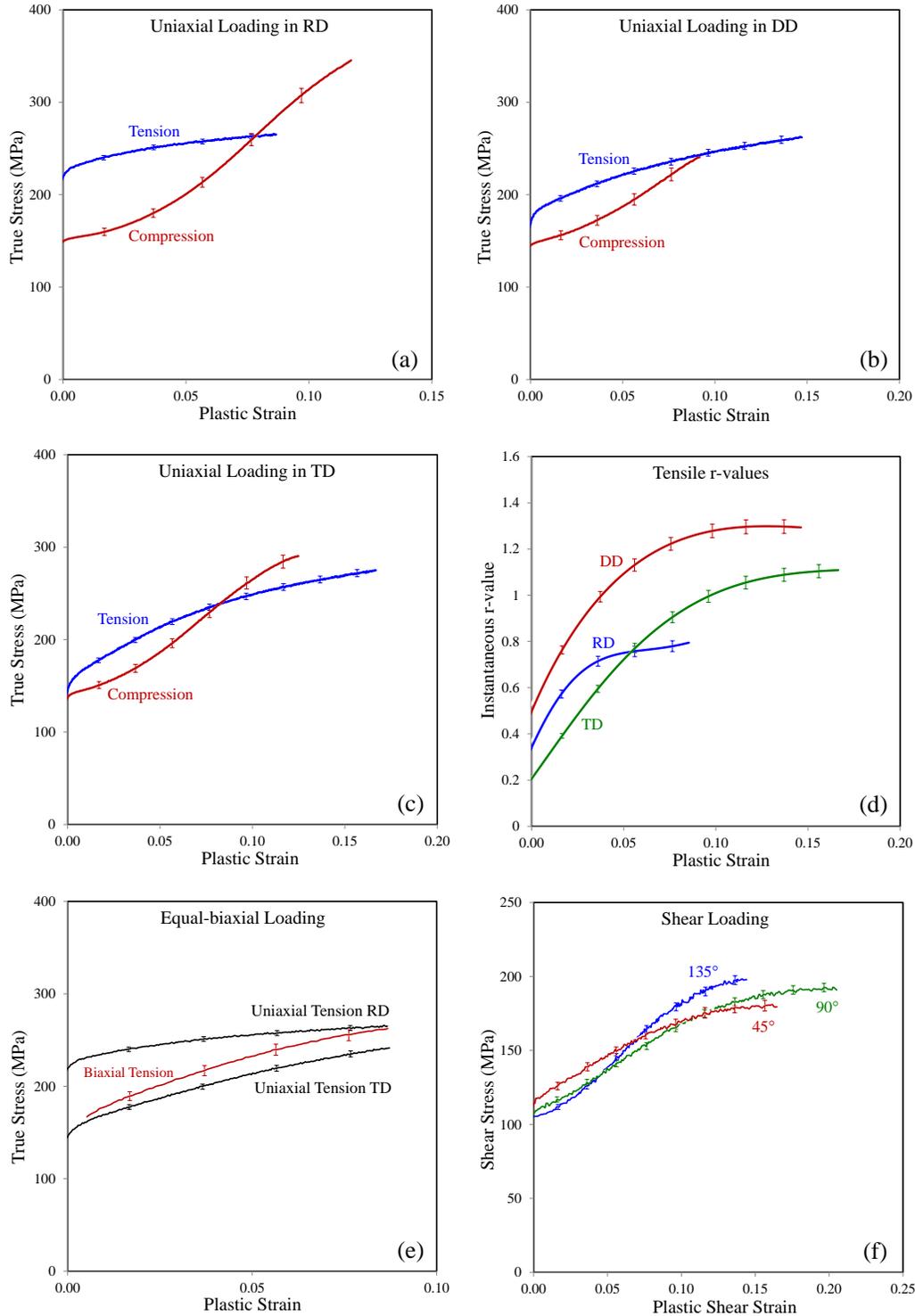
Figure 4.3 – Plastic response of ZEK100-O at room temperature under quasi-static strain rate of 0.001 s^{-1} for different loading conditions of (a) uniaxial loading in RD, (b) uniaxial loading in DD, (c) uniaxial loading in TD, (d) tensile r-values, (e) equal-biaxial tension, and (f) shear. The shear stress results are plotted with respect to the plastic component of shear strain.
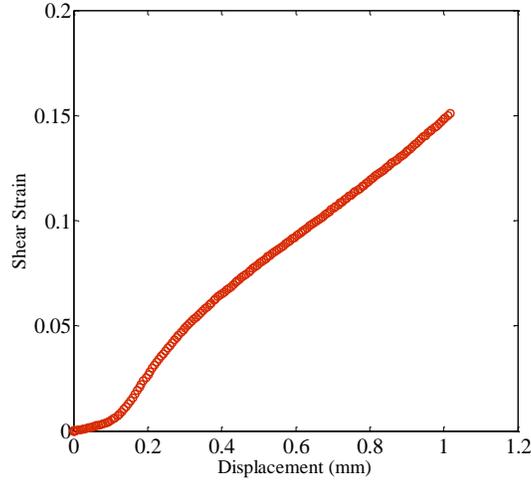
Figure 4.4 – DIC shear strain with respect to far-field displacement for a shear test in the 135° orientation.
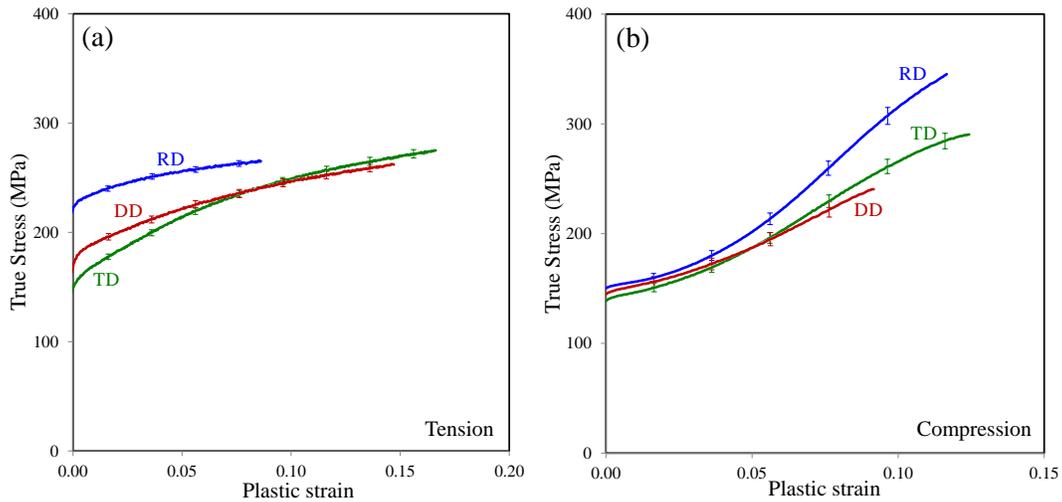
Figure 4.5 – (a) tension and (b) compression responses of ZEK100-O in different orientations.

In addition, it is shown in Appendix A that the plastic response obtained from shear tests in the 0° and 90° are almost identical while the responses in the 45° and 135° are significantly different, in contrast to common observations for orthotropic sheets. The reason behind similar responses in the 0° and 90° directions in shear state can be explained by considering an ideal shear loading condition for which the principal loading directions are offset by $\pm 45°$ relative to the applied shear loading direction with equal and opposite magnitudes. The Mohr's circles for applied shear loadings in the 0, 45°, 90° and 135° directions are presented in Figure 4.6 to demonstrate the principal stress magnitudes and directions and how these act on the various

material directions for each load orientation. For example, for the shear experiments with the applied load in the rolling direction (0°), the tensile component of the principal stress is in the 45° direction while the compressive component is in the 135° direction. The opposite condition holds for the shear tests loaded in the 90° orientation where the principal stress in the 45° direction is compressive and the principal stress in the 135° direction is tensile (see conditions 1 and 3 in Figure 4.6). The material has the same tensile/compressive properties in the 45° and 135° directions, and as a result, the shear responses in the 0° and 90° orientations should be identical.
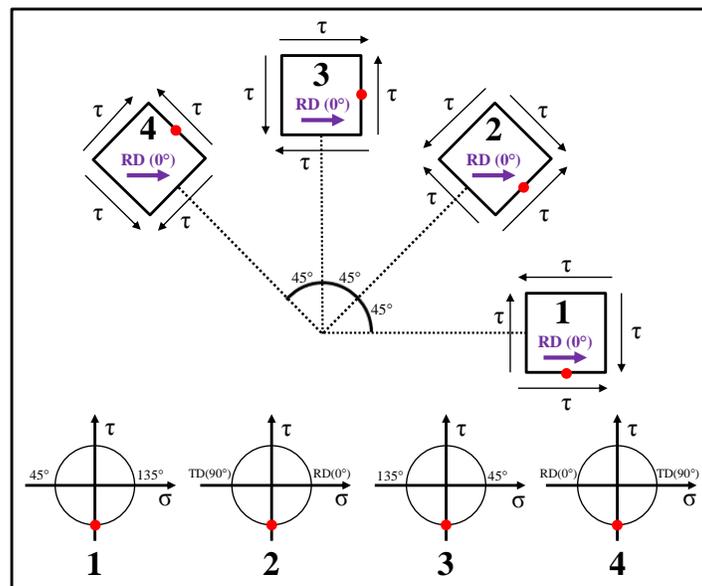
Figure 4.6 – Shear testing directions with their corresponding Mohr's circles.

When one considers the principal directions of the shear tests loaded in the 45° and 135° orientations, the tests in the 45° direction have a principal tensile component in the 0° and a compressive component in the 90°, whereas the shear tests in the 135° direction have a principal compressive component in 0° and a tensile component in the 90° (see conditions 2 and 4 in Figure 4.6). As shown earlier in Figures 4.3(a) and (c), ZEK100-O possesses a strong tension-compression asymmetry so that the response of the material in the rolling (0°) and transverse (90°) directions are significantly different in tension *versus* compression leading to the remarkable difference in the shear response of the material when loaded in the 45° *versus* the 135° directions. The above explanation is the underlying reason for the difference in the response

between the 45° and 135° directions shown in Figure 4.3(f). The principal stress directions and magnitudes are the same but the signs of the principal stresses are opposite which triggers the asymmetric response of the material. Furthermore, it is shown in Appendix A that the principal stresses for tests in the 45° and 135° directions are located within the second and fourth quadrants of yield *loci*. This key result demonstrates that in addition to an asymmetric response in the 1st and 3rd quadrants of yield *loci* (tensile and compressive regions), an additional asymmetry exists between the 2nd and 4th quadrants for magnesium alloys. Note that the deformation mechanisms accommodating plastic deformation are different for shear tests in the 45° and 135° directions and the activity of twinning mechanisms in each of these tests was quantitatively investigated using the EBSD analysis in Appendix A.

In summary, the experimental results presented in this section show the challenging nature of ZEK100-O in terms of modelling and characterization and highlight a need for accurate constitutive plasticity models that are able to capture the complex anisotropy and asymmetry of the material. This asymmetry is shown to extend to the 2nd and 4th quadrants of the yield *loci*. Development of a plasticity model capable of capturing these features is pursued in Section 4.2.

4.2. Phenomenological Plasticity Model

The experimental data presented in Section 4.1 has served to characterize the significant anisotropy present in the plastic response of ZEK100-O sheet and highlighted the need for accurate modelling approaches. To address this requirement, a phenomenological plasticity approach is adopted and developed in the present section. An overview of the modelling approach and resulting predictions are given in this section while more detailed explanations can be found in Appendix B.

4.2.1. Modelling Approach

The phenomenological yield criterion of CPB06 proposed by Cazacu *et al*. (2006) was adopted in the present study to investigate the yielding behaviour of ZEK100-O. In analogy to Plunkett *et al*. (2008), two linear stress transformations were performed to increase the degree of flexibility of the model, denoted as CPB06ex2, (see Eqs. 2.10-12 for formulation of the model).

The non-associative flow rule was employed in the present study with the same functional form as the yield function to define the plastic potential, Ψ, to which the plastic strain components are normal and their magnitudes are governed by:

$$d\boldsymbol{\varepsilon}^p = d\lambda \ \frac{\partial \Psi}{\partial \boldsymbol{\sigma}} \qquad (4.1)$$

where $d\boldsymbol{\varepsilon}^p$ is the increment of plastic strain tensor, and $d\lambda$ is the plastic multiplier. Using the principal of plastic work equivalence and assuming that the plastic potential is a first-order homogeneous function, the following relation can be used to calculate the equivalent plastic strain (Cvitanic *et al.,* 2008):

$$d\varepsilon^p_{eq} = d\lambda \ \frac{\Psi}{\Phi} \qquad (4.2)$$

in which Φ is the yield function. For the associative flow rule ($\Phi = \Psi$), Eq. (4.2) reduces to:

$$d\varepsilon^p_{eq} = d\lambda \qquad (4.3)$$

The values of the coefficients of transformation tensors and strength differential parameters (see Appendix B) can be determined from an optimization approach to minimize the errors between the experimental data and the values predicted by the yield function and plastic potential. In the present study, the genetic algorithm (GA) which is a global optimizer available in Matlab® was used to minimize "*Error*" given by:

$$Error = \sum_{i=1}^{j}\left(\left(\frac{\sigma^t_{CPB}}{\sigma^t_{exp}}\right)_i - 1\right)^2 + \sum_{i=1}^{k}\left(\left(\frac{\sigma^c_{CPB}}{\sigma^c_{exp}}\right)_i - 1\right)^2 + \sum_{i=1}^{l}\left(\left(\frac{\tau_{CPB}}{\tau_{exp}}\right)_i - 1\right)^2 + \sum_{i=1}^{j}\left(\left(\frac{r^t_{CPB}}{r^t_{exp}}\right)_i - 1\right)^2 \qquad (4.4)$$

where *j*, *k*, and *l* are the number of tensile, compressive, and shear stresses, respectively. Note that the superscripts *t* and *c* show the tension and compression values. In addition, the subscripts *exp* and *CPB* show whether the values are from experiments or from the model. To calibrate the plasticity model, seven uniaxial tensile yield stresses and r-values were used along with an equal-biaxial yield stress and r-value (*j*=8). Moreover, three uniaxial compression yield stresses (*k*=3), and three shear stresses (*l*=3) were utilized. Note that the first three terms in Eq. (4.4) are considered for calibrating the yield function while only the last term in Eq. (4.4) is needed to calibrate the plastic potential. In addition, the shear constrained proposed by Abedini *et al.* (2017b) was imposed on the plastic potential to obtain equal and opposite principal strains under shear state.

Since magnesium alloy exhibits an evolving anisotropic response, in the present study, the experimental values corresponding to nine levels of plastic work per unit volume, w^p, associated with equivalent plastic strains of 0.01 to 0.09 for uniaxial tension in reference direction of the RD were considered to calibrate the coefficients of the yield function and plastic potential. To determine the current yield function and plastic potential, an interpolation-based methodology described in Appendix B was adopted. Note that instead of interpolating the coefficients of the model, the yield function and plastic potential were interpolated directly to ensure that the shapes of *loci* are interpolated accurately. Also note that the upper bound value of the plastic work level for calibration of anisotropic yield function and plastic potential is limited by the onset of plastic instability (necking) for the tensile test in the RD direction which occurs at a strain of approximately 0.09. Due to this limitation, it was assumed that the shape of the yield *loci* and plastic potential remain constant after this level of plastic deformation. The model was

implemented into LS-DYNA as a user material subroutine (UMAT) for general 3-D stress states to better capture through-thickness stress and strain fields. More information regarding the numerical implementation and finite element discretization can be found in Appendix B.

4.2.2. Yield Function and Plastic Potential

The coefficients of the yield function and plastic potential of ZEK100-O at different plastic work levels were calibrated, and, for brevity, only three levels of plastic deformation are shown in this section (plastic work levels of 2.24 MJ/m^3, 14.61 MJ/m^3, and 22.46 MJ/m^3 associated with plastic strains of 0.01, 0.06, and 0.09, respectively). The prediction of the corresponding yield functions and plastic potentials are shown in Figures 4.7 to 4.9. It can be seen that the CPB06ex2 yield function and plastic potential can be fit to the measured data with good accuracy. For the smallest plastic work level of 2.24 MJ/m^3 which is close to the initial yielding of the material, it can be seen from Figure 4.7 that the material has a clear tension-compression asymmetry with the tension region having larger yield stresses than the compression region. The tension-compression asymmetry of yield *loci* reduces with deformation due to the high hardening rate in compression offsetting its initially lower yield strength with respect to tension as shown in Figure 4.8 for the plastic work level of 14.61 MJ/m^3. At the plastic work level of 22.46 MJ/m^3 (Figure 4.9) the yield stresses in compression have grown larger than in tension which is opposite to that observed for the material at the onset of yielding. Note that this material exhibits asymmetry not only in the tension-compression regions but also in the shear regions corresponding to the 2nd and 4th quadrants of the yield *loci*. This shear asymmetry correlates with the sign of the principal stresses acting under the shear state, activating different types of deformation mechanisms as described in Section 4.1.3.
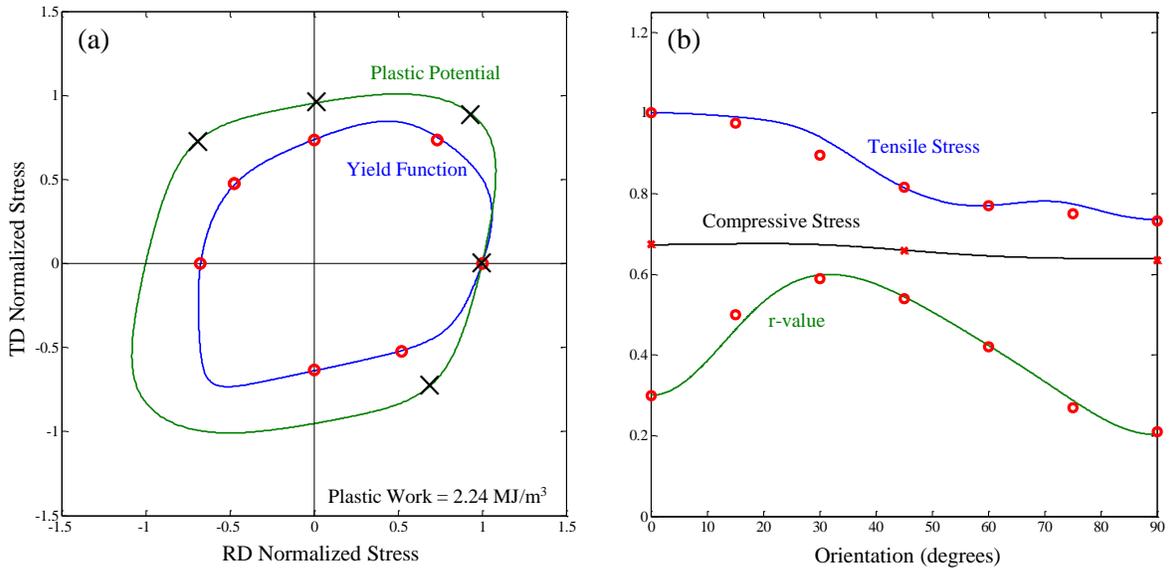
Figure 4.7 – (a) Yield function and plastic potential and (b) uniaxial yield stress ratios and r-values at a plastic work level of 2.24 MJ/m^3. Symbols show the experimental results. The symbol X was used to show the locations on the plastic potential where constraints were imposed.
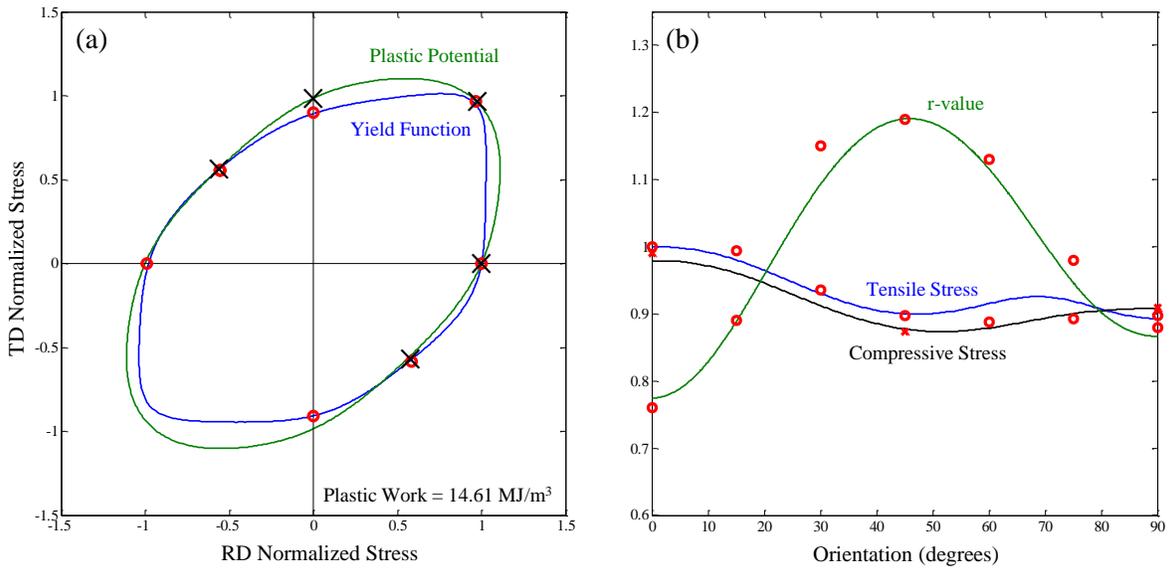
Figure 4.8 – (a) Yield function and plastic potential and (b) uniaxial yield stress ratios and r-values at a plastic work level of 14.61 MJ/m^3. Symbols show the experimental results. The symbol X was used to show the locations on the plastic potential where constraints were imposed.
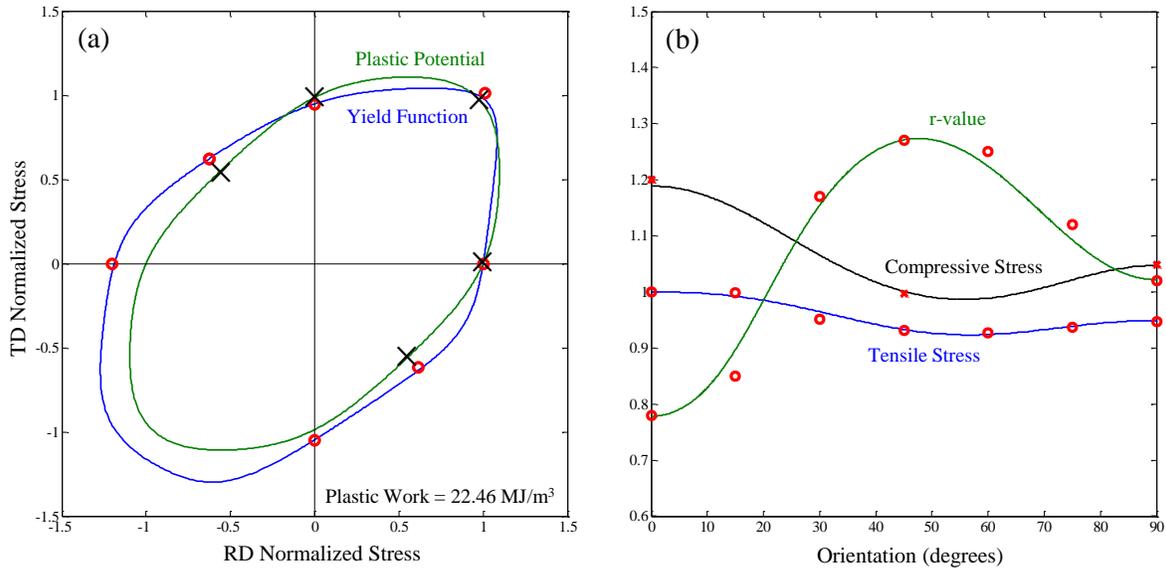
Figure 4.9 – (a) Yield function and plastic potential and (b) uniaxial yield stress ratios and r-values at a plastic work level of 22.46 MJ/m³. Symbols show the experimental results. The symbol X was used to show the locations on the plastic potential where constraints were imposed.

It is instructive to perform a comparison between the AFR and non-AFR frameworks in terms of their capabilities to capture the experimental data. Since the yield function and plastic potential in the non-AFR model each have two stress transformations (*i.e.* CPB06ex2), in order to provide a fair comparison, the AFR model was calibrated with four stress transformations (*i.e.* CPB06ex4) to have a similar number of calibration coefficients. The same calibration strategy described in Section 4.2.1 was used to obtain the coefficients of the CPB06ex4 model for a selected plastic work level of 22.46 MJ/m³ and its results are compared with that of the non-AFR model in Figure 4.10. It can be seen that the AFR model with four linear stress transformations can reproduce the experimental data with a reasonably good accuracy; however, the agreement is not as good as with the non-AFR model. Keeping in mind that the two models have a similar number of calibration coefficients, it is apparent that simply doubling the stress transformations from two to four in the AFR model, does not provide as good an agreement as the non-AFR using a separate two-transformation yield function and plastic potential. This further highlights the advantage of the non-AFR model for materials such as magnesium alloys with significant plastic anisotropy in which improved model flexibility can be achieved without the need to increase the number of calibration parameters.
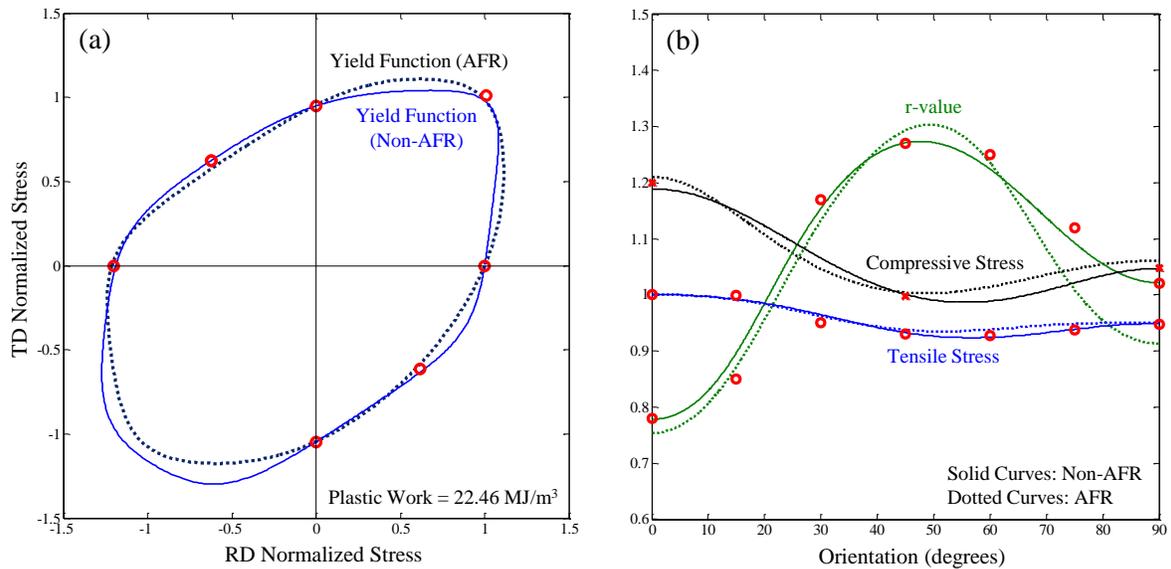
Figure 4.10 – (a) Yield function and (b) uniaxial yield stress ratios and r-values of AFR and non-AFR models at a plastic work level of 22.46 MJ/m³. Note that two separate stress transformations were used for the non-AFR yield function and flow potential (CPB06ex2), while four stress transformations were used for the AFR model (CPB06ex4). Symbols show the experimental results.

4.2.3. Finite Element Implementation

In order to evaluate the accuracy of the implemented plasticity model, simulations utilizing a single 3-D brick element under different proportional loading conditions were used to predict the stress-strain response and evolution of r-values of the material. An important advantage of single-element simulations is that any desired stress state can be achieved without structural complexities such as buckling, plastic instability, and necking. Figure 4.11 displays comparisons between predicted and measured results (see Section 4.1) under different stress states from which it can be seen that the model is capable of capturing the experimental trends with good accuracy. It can be observed from Figures 4.11(a-c) that the tension-compression asymmetric responses of the material in different orientations are reproduced with great accuracy. Also comparing to the experimental data, the model performs well under equal-biaxial tension and shear states, as shown in Figures 4.11(d) and (e), respectively. Moreover, the r-value evolutions are captured with reasonable accuracy in Figure 4.11(f). It should be noted that due to the inherent nature of the piece-wise linear interpolation approach, more accurate predictions can be achieved with

higher number of calibrations levels that leads to better numerical correlations at the cost of more expensive models.
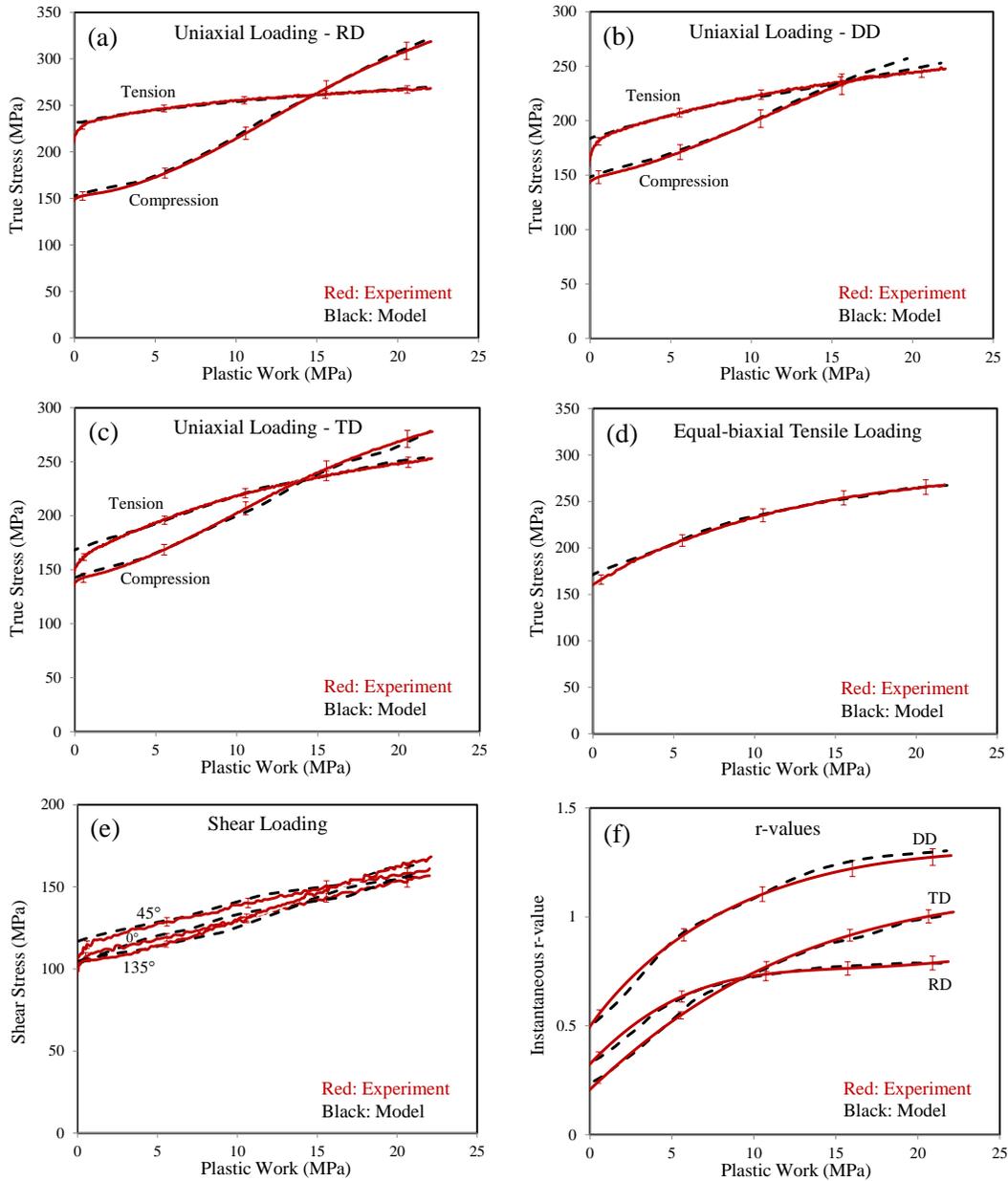
Figure 4.11 – Experimental data compared with predictions of a single-element model for uniaxial loading in (a) RD (b) DD, (c) TD, (d) equal-biaxial tension loading, (e) shear loading, and (f) uniaxial tensile instantaneous r-values.

Full-scale finite element simulations of selected experiments of hole tension, notch tension, plane-strain, and equal-biaxial dome tests, with specimen geometries depicted in Figures 4-12(a), (b), (c), and (d), respectively, were performed to evaluate the predictive capabilities of the

implemented non-AFR plasticity model. More information about these coupon-level tests is given in Section 4.3.1 and in detail in Appendix B. In these tests, the material undergoes different stress states that are commonly experienced in practical sheet metal forming operations and crash events. In the present section, the experimental and simulation data are compared in terms of global load-displacements while more detail concerning correlations between the model predictions and experiments including local strain values is given in Appendix B. Figures 4.13 and 4.14 compare the measured and predicted load-displacement responses of the in-plane tensile (hole tension and notch tension) and dome tests, respectively. The experimental data are plotted up to appearance of the first visible surface crack on the DIC images which is followed by a sudden load drop. In general, it can be seen that the agreement between the model and experiments are reasonably good for different test geometries and orientations.
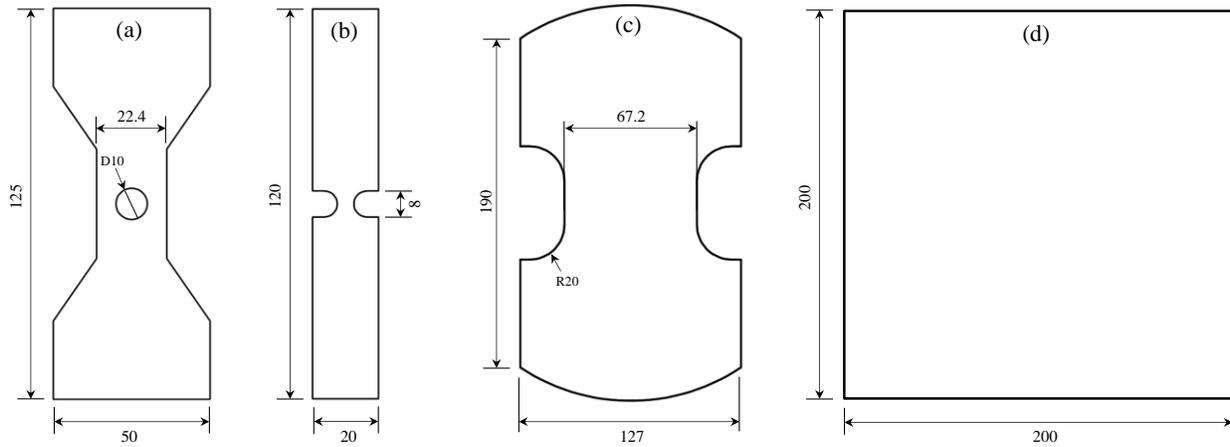
Figure 4.12 – Specimen geometries of (a) hole tension, (b) notch tension, (c) plane-strain dome, and (d) equal-biaxial dome tests. All dimensions are in millimetres.
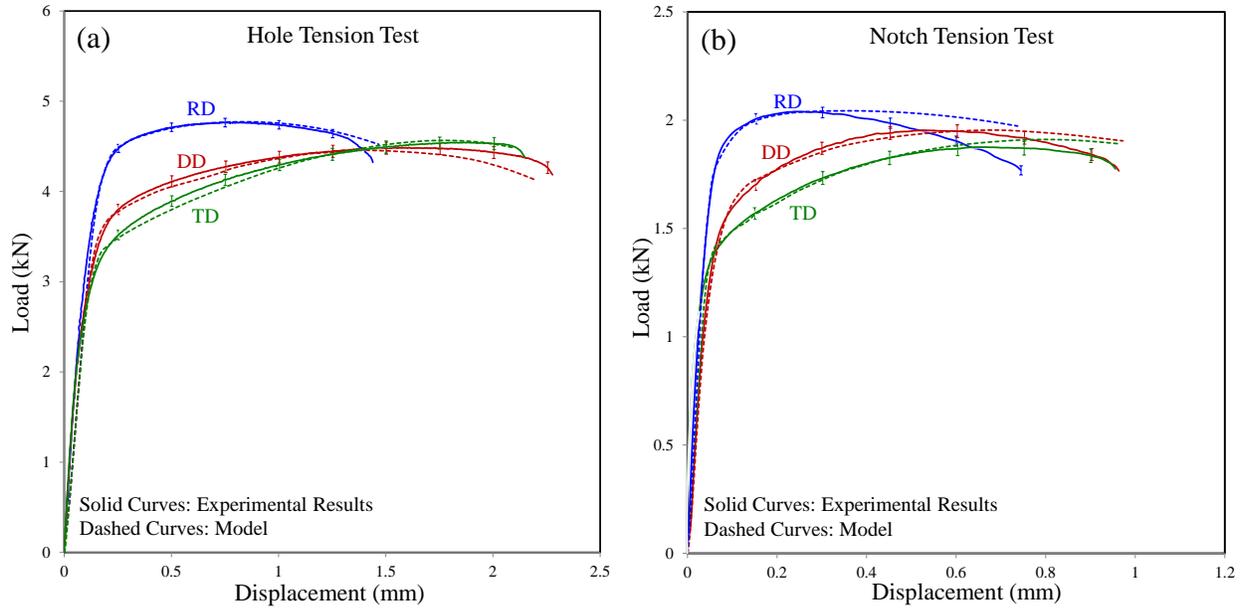
Figure 4.13 – Experimental data compared with predictions of the finite element model in terms of force-displacements for the in-plane tensile loadings of (a) hole tension, and (b) notch tension tests.
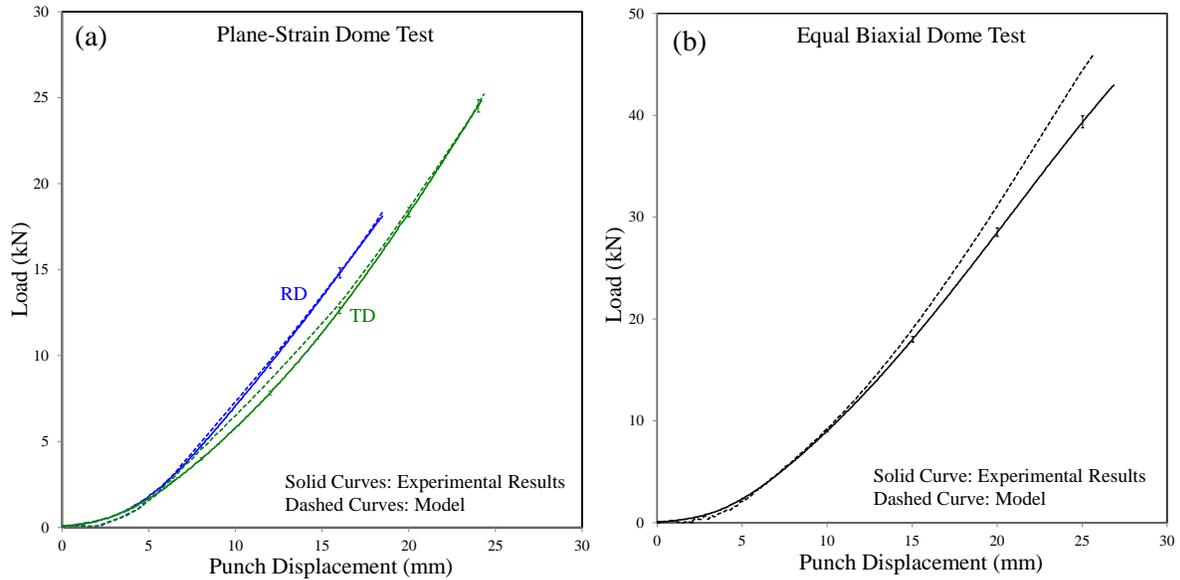
Figure 4.14 – Experimental data compared with the predictions of the finite element model in terms of the punch force-displacements for the dome tests with (a) plane-strain, and (b) equal-biaxial specimens.

It can be seen from Figure 4.13 that the correlations between the model and experiments are good for the hole tension and notch tension tests up to peak loads; however, after this point, the accuracy of the model deteriorates with further deformation which mostly leads to an over prediction of the applied forces. This discrepancy can be attributed to the hardening function or

to the extent of evolution of the plasticity model. For the hardening response, a Hockett-Sherby (Hockett and Sherby, 1975) equation was fit to uniaxial data in which for large strains (after necking) an area-reduction method was employed (see Appendix B). This procedure was followed by iteratively adjusting the flow curve in a finite element model of the tensile specimen until the measured and predicted load-displacement curves were matched; however, this approach does not guarantee that the hardening function is accurate. Also as mentioned earlier, the developed plasticity model evolves up to the limiting plastic work level of 22.46 MJ/m^3 (9% plastic strain for uniaxial tension test in the RD) after which the shapes of the yield function and plastic potential remain constant with further plastic deformation. After this point, the stress states deviate from the desired uniaxial loading. Nevertheless, it is expected that the anisotropy evolution or distortional hardening of the material persists in terms of the stress anisotropy after this point, however, this cannot be measured with the current characterization tests that are limited by the onset of plastic instability (necking).

In addition, it can be observed from Figure 4.14(a) that the punch force-displacements obtained from the finite element model are in accordance with the experimental results for the plane-strain dome tests in both orientations of the RD and TD. It should be noted that compared to the in-plane tensile tests, plane-strain dome tests result in relatively lower strains before fracture. It can be seen from Figure 4.14(b) that the model over predicts the punch force for the equal-biaxial dome test by approximately 12%. A large region of the dome specimen experiences the equal-biaxial tensile condition and in the plasticity model, this state of stress should be calibrated with great accuracy so that precise load-displacements can be obtained from the equal-biaxial dome test simulations. It can be seen from Figure 4.11(d) that the plasticity model is well-calibrated under this state of stress. Therefore, the discrepancy between the model and experiments might be related to the type of the characterization test (through-thickness compression test) that was used for the equal-biaxial condition. Obtaining the equal-biaxial tensile stress-strain response of sheet materials is difficult and the through-thickness compression test (*e.g.* Steglich *et al.*, 2014; Ghaffari Tari *et al.*, 2014) is used as an alternative to cruciform (*e.g.* Kuwabara *et al.*, 1998) or hydraulic bulge (*e.g.* Koc *et al.*, 2011) tests. For the magnesium alloy used in the present study, based on the predictions of the biaxial dome model, it appears that the through-thickness compression test overestimates the biaxial response of the material. It should be noted that the cruciform and bulge tests have their own shortcomings, for instance, the

cruciform test is only suitable for small plastic deformation and it requires complex specimen preparations (Bruschi *et al*., 2014), and the stress state in bulge tests is only approximately equal-biaxial (Aretz and Barlat, 2013). Keeping in mind these discrepancies, further investigations with other biaxial testing methods of cruciform and bulge tests are required to provide a better picture of the equal-biaxial response of the material.

4.3. Fracture Characterization

With the increased adoption of light-weight alloys for automotive structural components, significant weight reductions have been achieved; however, the fracture behaviour of these materials must be investigated to support predictions of their formability during manufacturing and fracture during crash events. It was observed in Section 4.1 that ZEK100-O sheet exhibits a significant evolving constitutive anisotropy and tension-compression asymmetry. The present section aims at characterizing the fracture behaviour of ZEK100-O under different stress states, as well as different test orientations with respect to the rolling direction of the sheet to assess fracture anisotropy.

4.3.1. Experiments and Methodology

The different types of specimens used for fracture characterization of ZEK100-O under various proportional loading conditions are shown in Figure 4.15. In the current experiments, the uniaxial tensile state was achieved with the hole tension specimen depicted in Figure 4.15(a). Typically, uniaxial tensile tests are performed with dogbone specimens; however, necking at low deformation levels limits their utility for studying fracture characterization at constant stress triaxiality. Compared to conventional dogbone specimens, the hole tension specimen shown in Figure 4.15(a) can delay the onset of necking and is a more representative test for fracture behaviour of materials under uniaxial tension conditions (Dunand and Mohr, 2010; Luo *et al*., 2012; Kofiani *et al*., 2013; Roth and Mohr, 2016).

Classical notch tensile tests (*e.g.* Dunand and Mohr, 2010; Lou and Yoon, 2017) were adopted to assess fracture strains at stress states between uniaxial and plane-strain tension. The notched specimen depicted in Figure 4.15(b) was utilized for in-plane experiments. The hole tension and notch tension tests were conducted in three orientations (RD, DD, and TD).
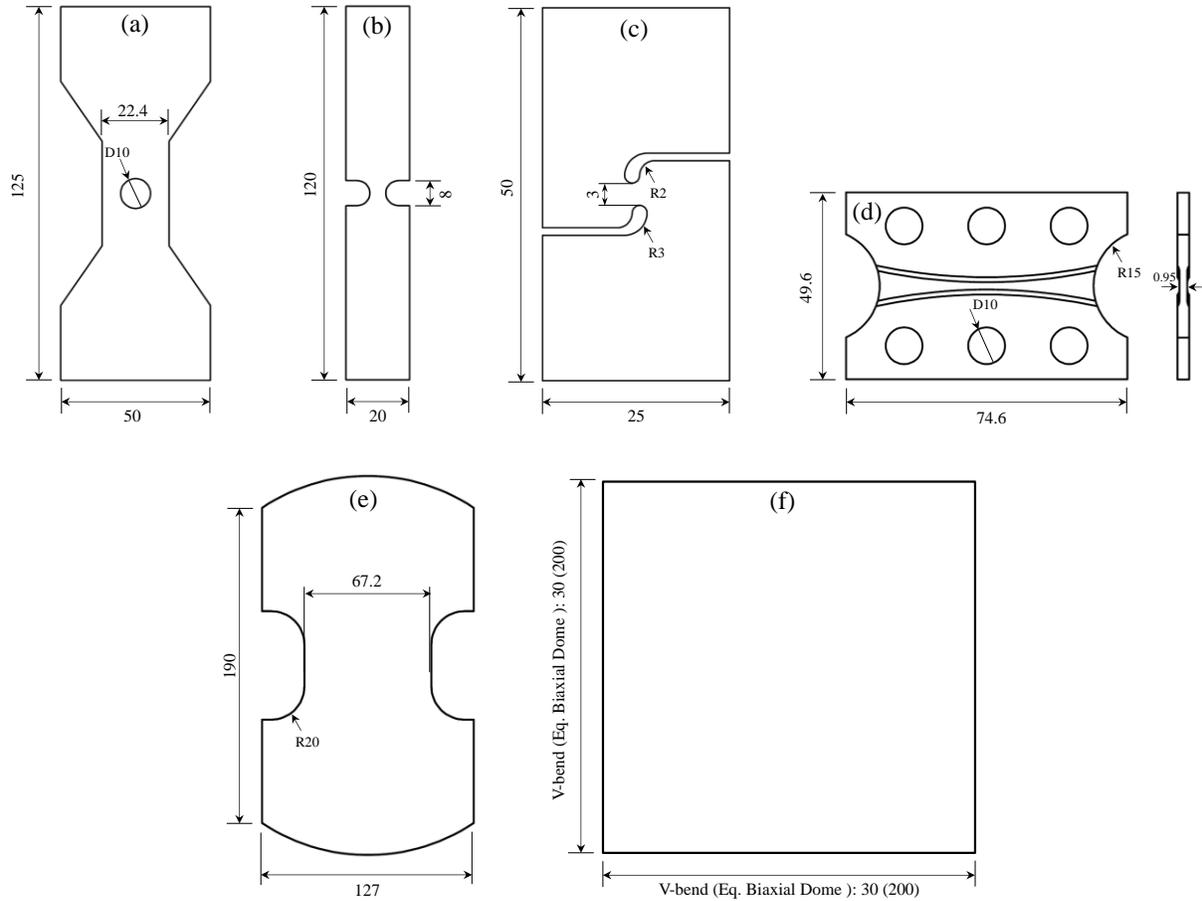
Figure 4.15 – Specimen geometries of (a) hole tension, (b) notch tension, (c) shear, (d) butterfly, (e) plane-strain dome, and (f) v-bend and equal-biaxial dome tests. All dimensions are in millimetres.

The shear specimen geometry (Figure 4.15c) employed for constitutive characterization (in Section 4.1) was also utilized to obtain the fracture response of the material under the shear state. In addition to this shear geometry, the butterfly specimen (Mohr and Henn, 2007; Dunand and Mohr, 2011) shown in Figure 4.15(d) was used to study the influence of the specimen geometry on shear fracture strains. More information on the butterfly testing is given in Appendix C. The shear tests were performed in three material directions (0° or RD, 45°, and 135°) with respect to the rolling direction. Note that the butterfly specimen can also be used to impose a plane-strain tension condition, as shown schematically in Figure 4.16. Due to the large gauge width of the specimen, the strain along the width direction is approximately zero at the center of the specimen. This state of stress is critical for formability and fracture characterization of sheet metals (Mahmudi, 2009). Three different types of plane-strain tests were considered in the

present study, namely, the plane-strain butterfly test, the hemispherical dome test, and tight-radius v-bend test shown in Figures 4.15(d), (e), and (f), respectively. The v-bend tests were done in the three directions of the RD, DD, and TD, while the plane-strain butterfly and dome tests were done in the RD and TD directions. All of these specimens possess wide gauge widths that facilitate achieving a plane-strain condition with zero in-plane minor strain at the center of the gauge area. Finally, testing under the equal-biaxial tension state was conducted using a hemispherical dome test with 200 mm×200 mm blanks depicted in Figure 4.15(f).
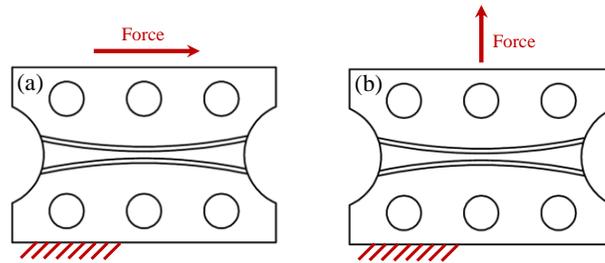
Figure 4.16 – Butterfly specimen under (a) shear, and (b) plane-strain tension states.

The experiments described above were performed with different types of equipment. The shear, hole tension, and notch tension tests were performed using a 100 kN MTS Criterion Model 45 servo-electric apparatus. The plane-strain butterfly test was performed with a butterfly rig (see Appendix C) and the plane-strain and equal-biaxial dome tests were conducted on a MTS formability press with tooling that conforms to the ISO12004-2 standard. Furthermore, the v-bend tests were done with a v-bend tester in which the custom-made apparatus allows for direct strain measurements (Cheong *et al.*, 2017) and the tests were performed according to the VDA 238-100 criterion utilizing a knife with a tip radius of 0.4 mm. Note that in all the tests in which tooling contact is required for deformation (dome and v-bend tests), Teflon® film lubricated with Vaseline® was used to reduce the influence of friction. The experimental tests described above were recorded using two digital cameras to obtain stereoscopic full-field logarithmic strains measurements using digital image correlation (DIC) techniques. To assess repeatability of the experimental results, at least four specimens were tested for each specimen geometry and orientation. More detail concerning the experimental methodology, DIC parameters, specimen preparations, and extracting fracture strains can be found in Appendices C and D.

4.3.2. Overview of Results (Proportional Conditions)

Figure 4.17 displays the measured DIC strain paths to fracture for selected specimens in which the anisotropy in the behaviour of the material along different orientations is apparent. The strain paths associated with isotropic materials are also plotted in Figure 4.17 for comparison. It can be seen that the responses are substantially different from isotropic conditions. In addition, significant deviation from $\varepsilon_1 = \varepsilon_2$ is observed for the equal-biaxial specimen that can be attributed to localization. To better visualize the anisotropy, the MMC phenomenological fracture curve (described in Appendix D) shown in Figure 4.18 was calibrated to the experimental data for loading along the RD, DD, and TD. When it comes to stress-state dependency, it can be seen from Figure 4.18 that the plane-strain tension condition has the lowest fracture strain closely followed by the shear state, while the material shows the highest ductility under the uniaxial tension condition for all orientations. In terms of anisotropy, it can be seen that the DD direction possesses the highest ductility while the fracture strains in the RD and TD directions are comparable. Anisotropy in fracture is the most significant under the uniaxial tension condition in which the DD direction displays approximately 20% higher ductility than the RD and TD directions, while the plane-strain condition exhibits a less significant directional sensitivity.
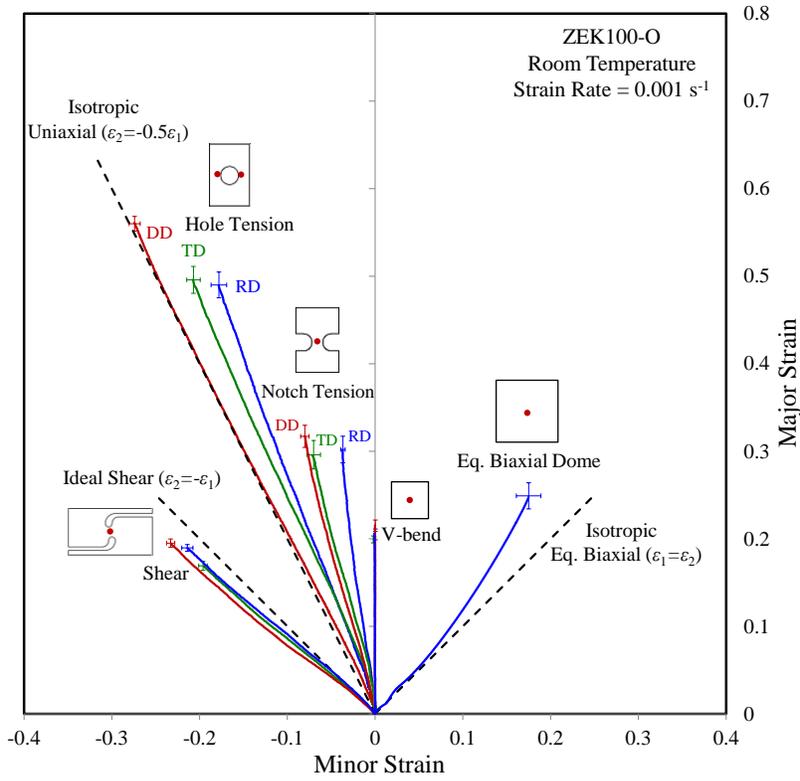
Figure 4.17 – Strain paths to fracture for different proportional tests. Strain paths for isotropic materials are also shown for comparison (black dashed lines).
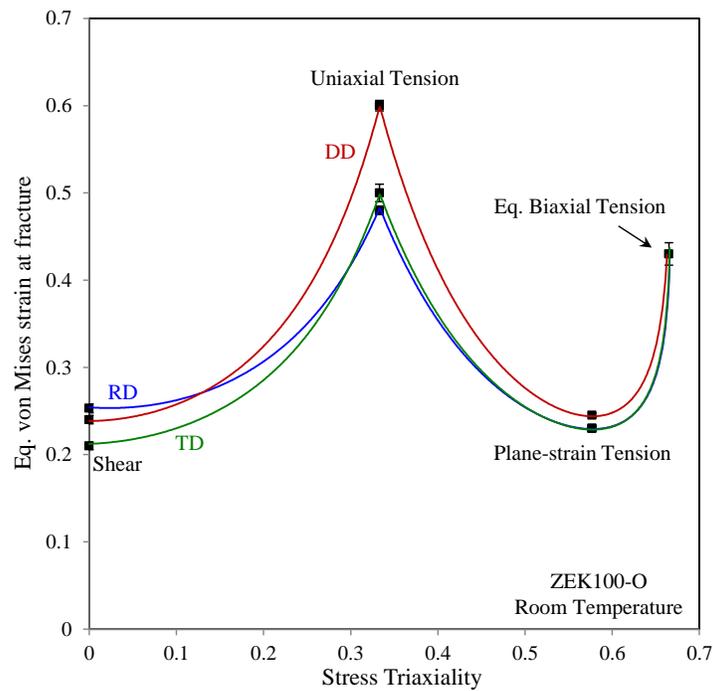
Figure 4.18 – MMC fracture *loci* under proportional loading conditions. Symbols and error bars show the experimental data.

Figure 4.19 compares the results of the shear specimen in Figure 4.15(c) and the butterfly specimen (Figure 4.15d). It can be seen that the butterfly specimen resulted in lower fracture strains with higher variations that could be the result of machining-induced defects during the through-thickness machining of the butterfly gauge region. Therefore, shear specimens without through-thickness machining are preferred for fracture characterization under shear loading conditions to reduce uncertainties and imperfections from the machining process. Furthermore, for materials with variation of properties through the sheet thickness, specimens with through-thickness machined regions characterize the sheet properties near the mid-plane, while specimens without through-thickness machining provide a more representative average response of the sheet in shear loading condition. Note that a similar behaviour was also observed in the shear response of a DP780 steel sheet with more detail provided in Appendix C.
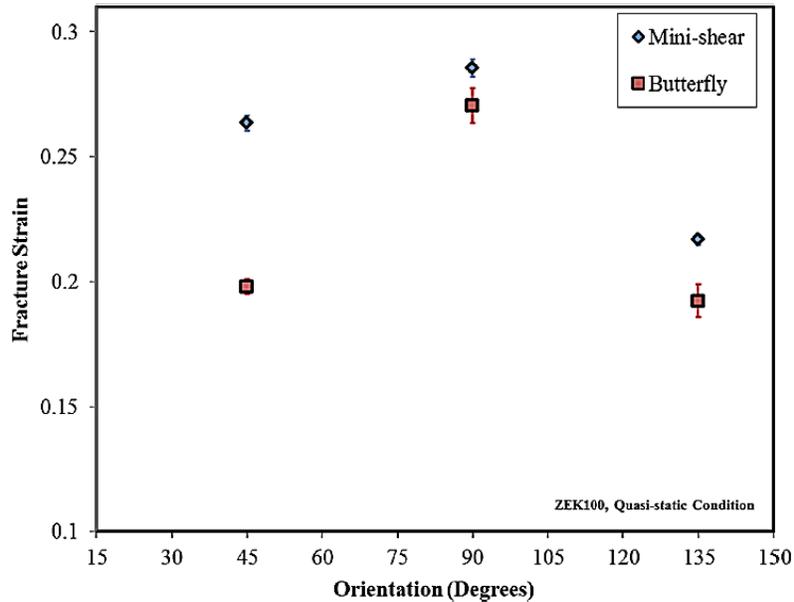
Figure 4.19 – Fracture strains obtained with different shear specimens. "Mini-shear specimen" refers to the specimen geometry depicted in Figure 4.15(c).

Due to the importance of the plane-strain state, strain paths of the plane-strain tests are compared in Figure 4.20. It can be seen that all of the tests lead to strain paths close to the desired plane-strain condition with relatively small minor strains. The strain path of the v-bend test lies almost perfectly on the zero minor strain line and the strain path of the butterfly test is close to the plane-strain condition; however, the plane-strain dome test shows some deviation

from an ideal plane-strain path for small deformation which is due to the biaxial bending associated with the dome radius (Hotz and Timm, 2008). Furthermore, in terms of the fracture strains in Figure 4.20, it can be observed that the v-bend test results in a higher fracture strain than the other two tests, specifically, the fracture strain is significantly higher than that of the plane-strain butterfly test. In a similar manner to the butterfly shear tests explained above, it is expected that the imperfections due to the through-thickness machining of the butterfly specimen are the underlying reason for lower fracture strains compared to the other plane-strain specimens.
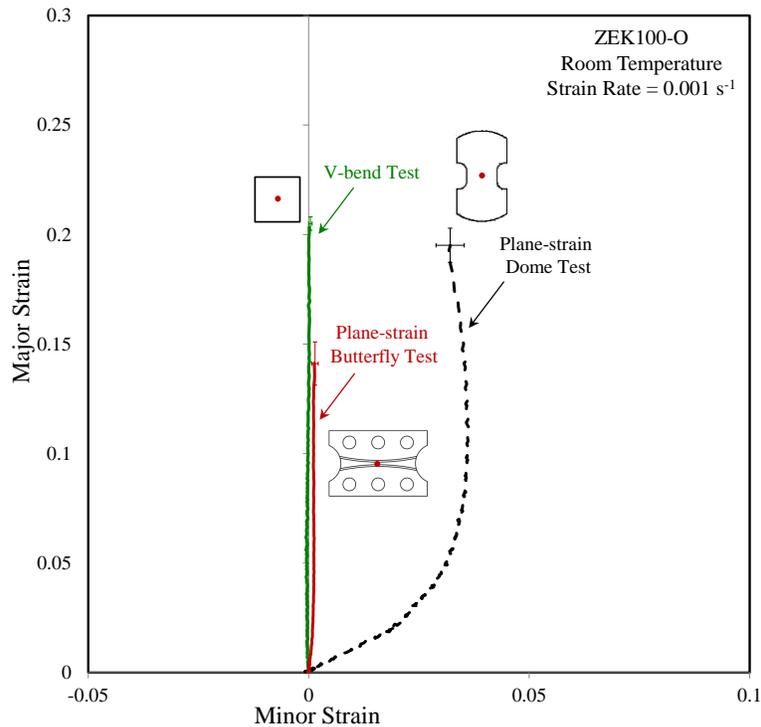
Figure 4.20 – Strain paths to fracture for different plane-strain tests. All the tests were performed in the RD.

4.3.3. Overview of Results (Non-proportional Conditions)

The understanding of behaviour of materials under non-proportional stress states is also essential since in forming operations and in crash events, materials are subjected to complex stress state changes. In the present research, in addition to proportional tests described in this section, fracture behaviour of ZEK100-O was evaluated under non-proportional conditions by pre-straining the material in uniaxial and equal-biaxial tension states to specific plastic work levels followed by abrupt changes of the stress states to plane-strain tension and shear (Table 4.2). For the first stage of the loading (pre-straining), two types of specimens were used: a

scaled-up tensile specimen and an equi-biaxial Marciniak specimen. The uniaxial tensile test was performed in the rolling direction of the sheet using the MTS tensile frame. The first stages of deformation with uniaxial and equi-biaxial tension states were stopped at a plastic work level of 22.46 MJ/m^3. This deformation level was chosen since it corresponds to the onset of necking in the uniaxial tension test in the RD, thus the two first stages of deformation were interrupted at the same plastic work level.

Figure 4.21 provides a concise summary of results of the non-proportional tests. These results suggest that the damage mechanisms responsible for fracture in the shear and plane-strain tension states are different such that only the damage mechanisms in the plane-strain condition were affected by pre-straining. In other words, the shear fracture response of the material after uniaxial or biaxial pre-straining is similar to the behaviour of the un-deformed material. In addition, pre-straining prior to the plane-strain tension tests results in different impacts on the fracture strains if the initial deformation is uniaxial or biaxial.

Moreover the results of the non-proportional tests were analyzed using a damage indicator relation in the form of Eq. (2.21) where different values of m=0.5, 1.0, 1.5 were considered (see also Figure 2.12) and the corresponding predictions are shown in Figure 4.21. It can be seen that increasing the value of the damage exponent leads to better fracture predictions for the shear state for both pre-straining conditions; however, the damage exponent of unity provides the best prediction for the plane-strain tension test after biaxial pre-straining. It is evident from the comparison between the model predictions and measured fracture strains that no one value of damage exponent can capture the measured trends. More discussion on this topic is provided in Appendix D.

Table 4.2 – Description of stress state change in non-proportional tests.
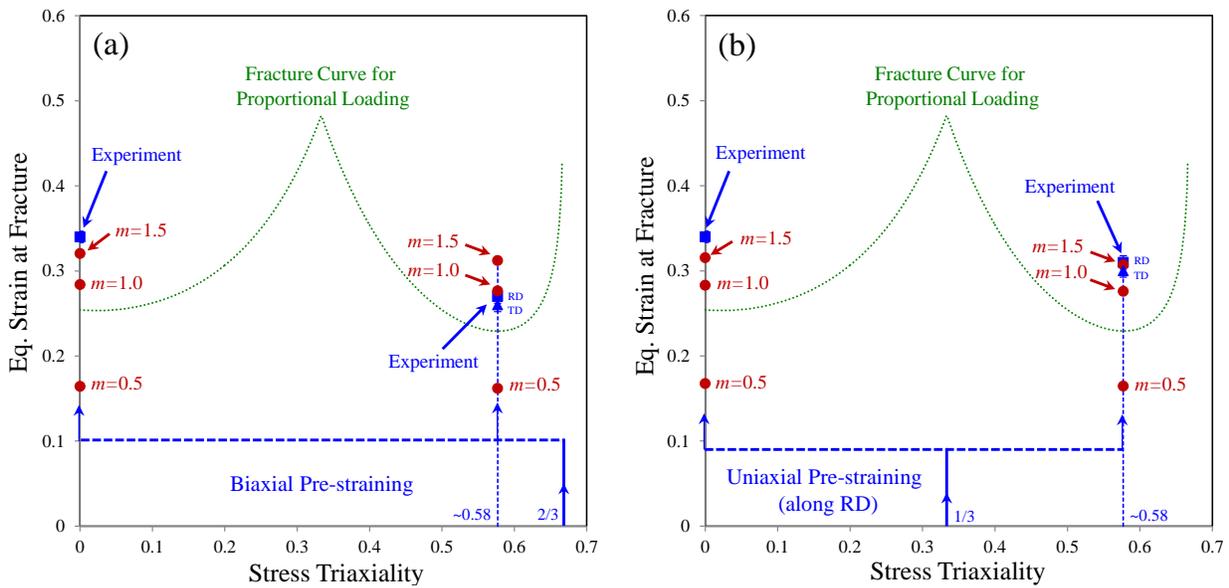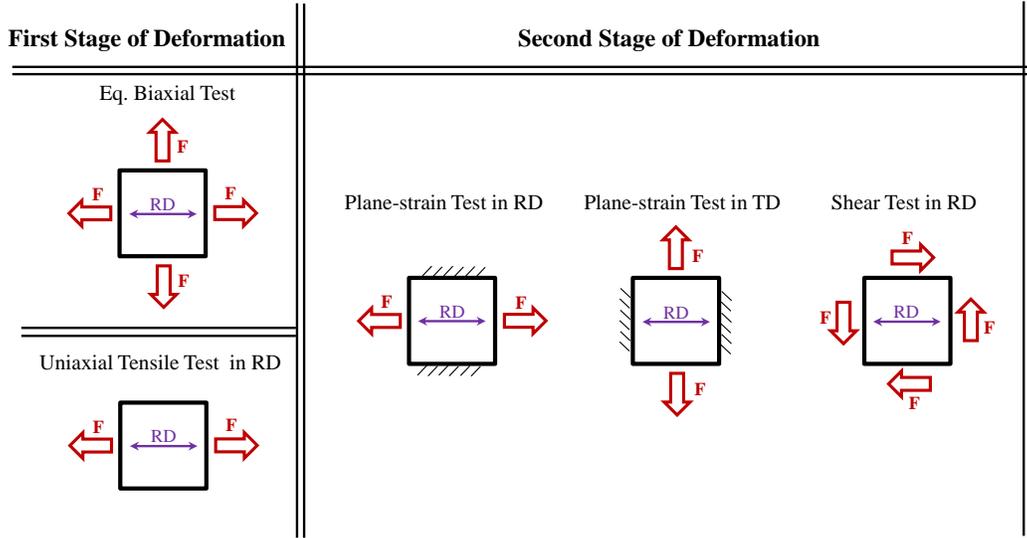
Figure 4.21 – Influence of the damage exponent, *m*, on non-proportional fracture predictions with (a) biaxial pre-straining and (b) uniaxial pre-straining (along RD). Load path histories are shown as blue curves. Predictions of fracture strain using the damage indicator approach for a range of damage exponents (*m* = 0.5, 1.0, 1.5) are plotted as red symbols and corresponding values of *m* are indicated. For reference, the proportional fracture *locus* in the RD is also plotted (green curve).

5. Summary

A detailed characterization of plasticity and fracture responses of ZEK100-O sheet at room temperature, under quasi-static conditions was performed. In particular, emphasis was placed on characterizing the complex evolving anisotropy and tension-compression asymmetry of the material. The r-values displayed evolving trends that suggested the evolution of the texture of the material with deformation. Furthermore, it was shown that the material exhibits asymmetry in the 2nd and 4th quadrants of yield *loci* in which the shear state dominates. The asymmetric behaviour is mostly attributed to activations of twinning mechanisms that accommodate plastic deformation. Moreover, the results of a comprehensive fracture testing program under different stress states and orientations showed a stress state dependent fracture response. It was revealed that the fracture response of the material is anisotropic, specifically in the uniaxial tension condition while the anisotropy in fracture was small under the plane-strain tension state.

An important achievement of this work was the development of a material model capable of considering evolving anisotropy/asymmetry of the magnesium alloy under proportional loading conditions. The non-associative flow rule was employed with the CPB06ex2 formulation along with an interpolation approach to capture the complex plastic response of ZEK100-O. Furthermore, it was shown that the flexibility of the non-AFR model to capture the experimental data is superior to that of the AFR model with the same number of calibration parameters. The model based on the non-AFR was implemented in LS-DYNA and validated using single-element and large-scale simulations. The results of the single-element simulations showed that the model was able to reproduce the experimental data used for calibration, and the results of the full-scale simulations of hole tension, notch tension, and dome tests showed that predictions of the model were in good agreement with experimental results in terms of both global and local responses. Thus, the current work demonstrated the advantages of employing a non-associative flow rule where its high flexibility facilitates capturing complex anisotropic responses as observed in magnesium alloys.

6. Conclusions

The following conclusions are drawn from this research:

- A strong evolving anisotropy and tension-compression asymmetry was observed in the plastic response of ZEK100-O rare-earth magnesium sheet, at room temperature, under quasi-static conditions. The r-values significantly evolved with plastic straining that suggests the evolution of the texture of the material with deformation. In addition to tension-compression asymmetry in the 1st and 3rd quadrants of the yield *loci*, an additional asymmetry in the shear zones corresponding to the 2nd and 4th quadrants of the yield *loci* was observed that was correlated to the underlying deformation mechanisms and was supported by the EBSD analysis.

- The CPB06ex2 criterion along with the non-associative flow rule with an interpolation technique was proven to be sufficiently flexible to capture the complex anisotropic response of ZEK100-O. This was achieved by enabling the possibility that the plastic potential and yield function evolve independently, a feature that is not possible in models based on the associative flow rule.

- A number of validation tests were selected to cover major stress states that are commonly encountered in forming operations and crash events. The validation tests included in-plane tensile and biaxial dome tests. Large-scale simulations of these experiments demonstrated that the plasticity model is capable of providing accurate predictions in terms of both global and local responses of the material.

- In addition to anisotropy in the plastic response, orientation-dependent fracture behaviour was revealed as a result of a comprehensive experimental program. However, compared to the severe anisotropy in plasticity, fracture anisotropy can be best characterized as moderate *albeit* non-negligible. The material displayed load-dependent fracture behaviour with the uniaxial tension state exhibiting the highest ductility.

- The results of non-proportional tests showed that employing simple damage indicators for phenomenological modelling of fracture might not be sufficient to capture the influence of severe changes in stress states.

7. Future Work

The following future work is proposed as next steps to strengthen the understanding of the behaviour of magnesium alloys and support their commercial implementation:

- The current investigations did not consider the plastic response of the material under non-proportional conditions. Under load reversal, twinned crystals may de-twin which may result in some specific features in the stress-strain behaviour of magnesium alloys (Abedini *et al*., 2016). Constitutive characterization and modelling of the plastic behaviour of magnesium alloys under non-proportional conditions is left for future work. It is expected that the non-proportional plasticity of ZEK100-O will be even more complex than its proportional behaviour and the modelling framework would have to be refined.

- The present work was mostly focused on plasticity and fracture of magnesium alloys from a macroscopic point of view. Microstructural investigations including crystal plasticity approaches and micromechanical fracture analysis with the aid of SEM should be performed in future work to connect the macroscopic responses to the underlying microscopic mechanisms. Specifically, it is of interest to study potential fracture mechanisms that are active under different loading conditions.

- The influence of strain rate and temperature on plasticity and fracture behaviour of ZEK100-O was not evaluated. A more comprehensive testing program including elevated strain rates and temperatures is the subject of future research. It is expected that the strain rate and temperature are coupled at elevated rates, thus the modelling efforts would require a fully coupled thermo-mechanical approach.

- The topic of modelling fracture behaviour of fracture-anisotropic metals has been barely touched in the literature. Results from the experiments performed in the present study showed the degree of anisotropy which exists in the fracture response of ZEK100-O; however, modelling this behaviour was left for future research.

- Fracture response of materials under combined loading of shear and tension is currently a topic of debate. For instance, when a material in the form of tube is under a combined tension and torsion, it may exhibit different fracture responses than previously observed for sheet materials (*e.g.* Scales *et al*., 2016). The behaviour of ZEK100-O under combined tension and shear states should be considered for future work.

References

Abedini A, Butcher C, Anderson D, Worswick M J, Skszek T, Fracture characterization of automotive alloys in shear loading, *SAE International Journal of Materials and Manufacturing*, 2015, **8**(3).

Abedini A, Butcher C, Worswick M J, Skszek T, Constitutive response of a rare-earth magnesium alloy sheet in monotonic and cyclic loadings, *Proceedings of 24th ICTAM conference*, 2016.

Abedini A, Butcher C, Nemcko M J, Kurukuri S, Worswick M J, Constitutive characterization of a rare-earth magnesium alloy sheet (ZEK100-O) in shear loading: studies of anisotropy and rate sensitivity, *International Journal of Mechanical Sciences*, 2017a, **128-129**:54-69.

Abedini A, Butcher C, Rahmaan T, Worswick M J, Evaluation and calibration of anisotropic yield criteria in shear loading: Constraints to eliminate numerical artefacts, *International Journal of Solids and Structures*, 2017b, http://dx.doi.org/10.1016/j.ijsolstr.2017.06.029.

Abedini A, Butcher C, Worswick M J, Fracture characterization of rolled sheet alloys in shear loading: Studies of specimen geometries, anisotropy, and rate sensitivity, *Experimental Mechanics*, 2017c, **57**:75-88.

Agnew S R, Duygulu O, Plastic anisotropy and the role of non-basal slip in magnesium alloy AZ31B, 2005, *International Journal of Plasticity*, **21**:1161-1193.

Allahverdizadeh N, Manes A, Giglio M, Identification of damage parameters for Ti-6Al-4V titanium alloy using continuum damage mechanics, *Mat. wiss. U Werkstofftech*, 2012, **45**:5-15.

Andar M O, Kuwabara T, Steglich D, Material modeling of AZ31 Mg sheet considering variation of r-values and asymmetry of the yield *locus*, *Material Science and Engineering A*, 2012, **549**:82-92.

Aretz H, Barlat F, New convex yield functions for orthotropic metal plasticity, *International Journal of Non-linear Mechanics*, 2013, **51**:97-111.

Athale M, Gupta A K, Singh S K, Vaidyanathan A, Analytical and finite element simulation studies on earing profile of Ti-6Al-4V deep drawn cups at elevated temperatures, *International Journal of Material Forming*, 2017, DOI: 10.1007/s12289-017-1358-3.

Bai Y, Wierzbicki T, A new model of metal plasticity and fracture with pressure and Lode dependence, *International Journal of Plasticity*, 2008, **24**:1071-1096.

Bai Y, Wierzbicki T, Application of extended Mohr-Coulomb criterion to ductile fracture, *International Journal of Fracture*, 2010, **161**:1-20.

Bao Y, Wierzbicki T, On fracture *locus* in the equivalent strain and stress triaxiality space, *International Journal of Mechanical Sciences*, 2004, **46**(1):81-98.

Bao Y, Treitler R, Ductile crack formation on notched AA2024-T351 bars under compression-tension loading, *Materials Science and Engineering A*, 2004, **384**(1-2):385-394.

Barlat F, Richmond O, Prediction of tricomponent plane stress yield surfaces and associated flow and failure behaviour of strongly textured f.c.c polycrystalline sheets, *Material Science and Engineering*, 1987, **95**:15-29.

Barlat F, Lian K, Plastic behavior and stretchability of sheet metals. Part I: a yield function for orthotropic sheets under plane stress conditions, *International Journal of Plasticity*, 1989, **5**:51-66.

Barlat F, Lege D J, Brem J C, A 6-component yield function for anisotropic materials, *International Journal of Plasticity*, 1991, **7**:693-712.

Barlat F, Maeda Y, Chung K, Yanagawa M, Brem J C, Hayashida Y, Lege D J, Matsui K, Murtha S J, Hattori S, Becker R C, Makosey S, Yield function development for aluminum alloy sheets, *Journal of Mechanics of Physics and Solids*, 1997, **45**:1727-1763.

Barlat F, Brem J C, Yoon J W, Chung K, Dick R E, Lege D J, Pourboghrat F, Choi S H, Chu E, Plane stress yield function for aluminum alloy sheets – part I: theory, *International Journal of Plasticity*, 2003, **19**:1297-1319.

Barlat F, Aretz H, Yoon J W, Karabin M E, Brem J C, Dick R E, Linear transformation-based anisotropic yield functions, *International Journal of Plasticity*, 2005, **21**:1009-1039.

Barlat F, Gracio J J, Lee M, Rauch E F, Vincze G, An alternative to kinematic hardening in classical plasticity, *International Journal of Plasticity*, 2011, **27**:1309-1327.

Barlat F, Jeong Y, Ha J, Tome C, Lee M, Wen W, Advances in constitutive modeling of plasticity for forming applications, *Key Engineering Materials*, 2017, **725**:3-14.

Barros P D, Alves J L, Oliveira M C, Menezes L F, Modeling of tension-compression asymmetry and orthotropy on metallic materials: Numerical implementation and validation, *International Journal of Mechanical Sciences*, 2016, **114**:217-232.

Basu S, Benzerga A A, On the path-dependence of the fracture *locus* in ductile fracture: Experiments, *International Journal of Solids and Structures*, 2015, **71**:79-90.

Bishop J F W, Hill R, A theory of the plastic distortion of a polycrystalline aggregate under combined stresses, *Philosophical Magazine*, 1951, **42**:414-427.

Boba, M., Butcher, C., Panahi, N., Worswick, M.J., Mishra, R., Carter, J., Formability of magnesium-rare earth alloy ZEK100 sheet at elevated temperatures, *International Journal of Material Forming*, 2017, **10**:181–191.

Brunig M, Gerke S, Hagenbrock V, Micro-mechanical studies on the effect of the stress triaxiality and the Lode parameter on ductile damage, *International Journal of Plasticity*, 2013, **50**:49-65.

Bruschi S, Altan T, Banabic D, Bariani P F, Brosius A, Cao J, Ghiotti A, Khraishesh M, Merklein M, Tekkaya A E, Testing and modelling of material behaviour and formability in sheet metal forming, *CIRP Annals – Manufacturing Technology*, 2014, **63**:727-749.

Cazacu O, Barlat F, A criterion for description of anisotropy and yield differential effects in pressure-insensitive metals, *International Journal of Plasticity*, 2004, **20**:2027-2045.

Cazacu O, Plunkett B, Barlat F, Orthotropic yield criterion for hexagonal closed packed metals, *International Journal of Plasticity*, 2006, **22**:1171-1194.

Chaboche J L, A review of some plasticity and viscoplasticity constitutive theories, *International Journal of Plasticity*, 2008, **24**:1642-1693.

Chen Z T, The role of heterogeneous particle distribution in the prediction of ductile fracture, Ph.D. thesis, University of Waterloo, 2004.

Cheong K, Omer K, Butcher C, George R, Dykeman J, Evaluation of the VDA 238-100 tight radius bending tests using digital image correlation strain measurement, *Proceedings of IDDRG 2017*.

Chu C, Needleman A, Void nucleation effects in biaxially stretched sheets, *Journal of Engineering Materials and Technology*, 1980, **102**:249-256.

Chung K, Ma N, Park T, Kim D, Yoo D, Kim C, A modified damage model for advanced high strength steel sheets, *International Journal of Plasticity*, 2011, **27**:1485-1511.

Clift S E, Hartley P, Sturgess C E N, Rowe G W, Fracture prediction in plastic deformation processes, *International Journal of Mechanical Science*, 1990, **32**:1-17.

Coer J, Laurent H, Oliveira M C, Manach P Y, Menezes L F, Detailed experimental and numerical analysis of a cylindrical cup deep drawing: Pros and cons of using solid-shell elements, *International Journal of Material Forming*, 2017, DOI: 10.1007/s12289-017-1357-4.

Cvitanic V, Vlak F, Lozina Z, A finite element formulation based on non-associated plasticity for sheet metal forming, *International Journal of Plasticity*, 2008, **24**:646-687.

Drucker D C, Relation of experiments to mathematical theories of plasticity, *Journal of Applied Mechanics*, 1949, **16**:349-357.

Dunand M, Mohr D, Hybrid experimental-numerical analysis of basic ductile fracture experiments for sheet metals*, International Journal of Solids and Structures*, 2010, **47**:1130-1143.

Dunand M, Mohr D, Optimized butterfly specimen for the fracture testing of sheet materials under combined normal and shear loading, *Engineering Fracture Mechanics*, 2011, **78**:2919-2934.

Fourmeau M, Borvik T, Benallal A, Lademo O G, Hopperstad O S, On the plastic anisotropy of an aluminum alloy and its influence on the constrained multiaxial flow, *International Journal of Plasticity*, 2011, **27**:2005-2025.

Fourmeau M, Borvik T, Benallal A, Hopperstad O S, Anisotropic failure modes of high-strength aluminum alloy under various stress states, *International Journal of Plasticity*, 2013, **48**:34-53.

Ghaffari Tari D, Worswick M J, Winkler S, Experimental studies of deep drawing of AZ31B magnesium alloy sheet under various thermal conditions, *Journal of Materials Processing Technology*, 2013, **213**:1337-1374.

Ghaffari Tari D, Worswick M J, Ali U, Gharghouri M A, Mechanical response of AZ31B magnesium alloy: Experimental characterization and material modeling considering proportional loading at room temperature, *International Journal of Plasticity*, 2014, **55**:247-267.

Ghahremaninezhad A, Ravi-Chandar K, Crack nucleation from a notch in a ductile material under shear dominant loading, *International Journal of Fracture*, 2013, **184**:253-266.

Gologanu M, Leblond M, Devaux J, Approximate models for ductile metals containing non-spherical voids – case of axisymmetric prolate ellipsoidal cavities, *Journal of Mechanics and Physics of Solids*, 1993, **41**:1723-1754.

Gologanu M, Leblond M, Devaux J, Approximate models for ductile metals containing non-spherical voids – case of axisymmetric oblate ellipsoidal cavities, *Journal of Engineering Materials and Technology*, 1994, **116**:290-297.

Grytten F, Holmedal B, Hopperstad O S, Borvik T, Evaluation of identification methods for YLD2004-18p, *International Journal of Plasticity*, 2008, **24**:2248-2277.

Gurson A L, Continuum theory of ductile rupture by void nucleation and growth – part I. Yield criteria and flow rules for porous ductile media, *Journal of Engineering Materials and Technology*, 1977, **99**:2-15.

Hockett J E, Sherby O D (1975), Large strain deformation of polycrystalline metals at low homologous temperatures, *Journal of Mechanics of Physics and Solids*, **23**:87-98.

Haltom S S, Kyriakides S, Ravi-Chandar K, Ductile failure under combined shear and tension, International Journal of Solids and Structures, 2013, **50**:1507-1522.

Hancock J W, Mackenzie A C, On the mechanisms of ductile failure in high-strength steels subjected to multi-axial stress-states, *Journal of Mechanics of Physics and Solids*, 1976, **24**:147-169.

Habib S A, Khan A S, Gnaupel-Herold T, Lloyd J T, Schoenfeld S E, Anisotropy, tension-compression asymmetry and texture evolution of a rare-earth-containing magnesium alloy sheet, ZEK100, at different strain rates and temperatures: experiments and modeling, *International Journal of Plasticity*, 2017, **95**:163-190.

Hershey A V, the plasticity of an isotropic aggregate of anisotropic face centered cubic crystals, *Journal of Applied Mechanics Transactions*, 1954, **21**:241-245.

Hill R, A theory of the yielding and plastic flow of anisotropic metals, *Proceeding of the Royal Society of London A*, 1948, **193**:281-297.

Hill R, Theoretical plasticity of textured aggregates, *Mathematical Proceedings of the Cambridge Philosophical Society*, 1979, **85**(1):179-191.

Hill R, Constitutive modelling of orthotropic plasticity in sheet metals, *Journal of Mechanics and Physics of Solids*, 1990, **38**:405-417.

Hill R, A user-friendly theory of orthotropic plasticity in sheet metals, *International Journal of Mechanical Sciences*, 1993, **35**:19-25.

Hippke H, Manopulo N, Yoon J W, Hora P, On the efficiency and accuracy of stress integration algorithms for constitutive models based on non-associated flow rule, *International Journal of Material Forming*, 2017, DOI: 0.1007/s12289-017-1347-6.

Hosford W F, A generalized isotropic yield criterion, *Journal of Applied Mechanics*, 1972, **39**:607-609.

Hotz W, Timm J, Experimental determination of forming limit curves (FLC). *Proceedings of the 7th Numisheet Conference*, 2008, 271-278.

Huh J, Huh H, Lee C S, Effect of strain rate on plastic anisotropy of advanced high strength steel sheets, *International Journal of Plasticity*, 2013, **44**:23-46.

Imandoust A, Barrett C D, Al-Samman T, Inal K A, El Kadiri H, A review of the effect of rare-earth elements on texture evolution during processing of magnesium alloys, *Journal of Materials Science*, 2017, **52**:1-29.

Inal K, Wu P D, Neale K W, Large strain behaviour of aluminum sheets subjected to in-plane simple shear, *Modelling and Simulation in Materials Science and Engineering*, 2002, **10**:237-252.

Jian A, Agnew S R, Modeling the temperature dependent effect of the twinning on the behavior of magnesium alloy AZ31B sheet, *Material Science and Engineering A*, 2007, **462**:29-36.

Jia Y, Bai Y, Experimental study on the mechanical properties of AZ31B-H24 magnesium alloy sheets under various loading conditions, *International Journal of Fracture*, 2016, **197**:25-48.

Kachanov L, On creep rupture time, Proceedings of the Academy of Sciences USSR Division of *Engineering Science*, 1958, **8**:2631-2651.

Khan A S, Pandey A, Gnaupel-Herold T, Mishra R J, Mechanical response and texture evolution of AZ31 alloy at large strains for different strain rates and temperatures, *International Journal of Plasticity*, 2011, **27**:688-706.

Kaya S, Altan T, Groche P, Klopsch C, Determination of the flow stress of magnesium AZ31-O sheet at elevated temperatures using hydraulic bulge test, *International Journal of Machine Tools & Manufacture*, 2008, **48**:550-557.

Kim N J, Critical assessment 6: magnesium sheet alloys: viable alternatives to steels?, *Material Science and Technology*, 2014, **30**(15):1925-1928.

Kofiani K, Nonn A, Wierzbicki T, New Calibration method for high and low triaxiality and validation on SENT specimens of API X70, *International Journal of Pressure Vessels and Piping*, 2013, **111-112**:187-201.

Kohar C P, Brahme A, Imbert J, Mishra R K, Inal K, Effects of coupling anisotropic yield functions with the optimization process of extruded aluminum front rail geometries in crashworthiness, *International Journal of Solids and Structures*, 2017, DOI: 10.1016/j.ijsolstr.2017.08.026.

Koc M, Billur E, Cora O N, An experimental study on the comparative assessment of hydraulic bulge test analysis and methods, *Materials and Design*, 2011, **32**:272-281.

Kurukuri S, Worswick M J, Ghaffari Tari D, Mishra R K, Carter J T, Rare-sensitivity and tension-compression asymmetry in AZ31B magnesium alloy sheet, *Philosophical Transactions of the Royal Society A*, 2014a, **372**:20130216.

Kurukuri S, Worswick M J, Bardelcik A, Mishra R K, Carter J T, Constitutive behavior of commercial grade ZEK100 magnesium alloy sheet over a wide range of strain rates. *Metallurgical and Materials Transactions A*, 2014b, **45**:3321-3337.

Kuwabara T, Ikeda S, Kuroda K, Measurement and analysis of differential work hardening in cold-rolled steel sheet under biaxial tension, *Journal of Materials Processing Technology*, 1998, **80-81**:517-523.

Kim J, Ryou H, Kim D, Kim D, Lee W, Hong S, Chung K, Constitutive law for AZ31B Mg alloy sheets and finite element simulation for three-point bending, *International Journal of Mechanical Sciences*, 2008, **50**:1510-1518.

Lemaitre J, A continuous damage mechanics model for ductile fracture, *Journal of Engineering Materials and Technology*, 1985, **107**:83-89.

Levesque J, Inal K, Neale K W, Mishra R K, Numerical modeling of formability of extruded magnesium alloy tubes, *International Journal of Plasticity*, 2010, **26**:65-83.

Lou X Y, Li M, Boger R K, Agnew S R, Wagoner R H, Hardening evolution of AZ31B Mg sheet, 2007, *International Journal of Plasticity*, **23**:44-86.

Lou Y, Yoon J W, Anisotropic ductile fracture criterion based on linear transformation, *International Journal of Plasticity*, 2017, **93**:3-25.

Luo M, Dunand M, Mohr D, Experimental and modeling of anisotropic extrusions under multi-axial loading – Part II: ductile fracture, *International Journal of Plasticity*, 2012, **32**:36-58.

Marcadet S J, Mohr D, Effect of compression-tension loading reversal on the strain to fracture of dual phase steel sheets, *International Journal of Plasticity*, 2015, **72**:21-43.

McClintock F, A criterion for ductile fracture by the growth of holes, *Journal of Applied Mechanics*, 1968, **35**:363-371.

Mahmudi R, A novel technique for plane-strain tension testing of sheet metals, *Journal of Material Processing Technology*, 1999, **86**:237-244.

Manopulo N, Peters P, Hora P, Assessment of anisotropic hardening models for conventional deep drawing processes, *International Journal of Material Forming*, 2017, DOI: 10.1007/s12289-016-1306-7.

Mirone G, Coralo D, Stress-strain and ductile fracture characterization of an X100 anisotropic steel: experiments and modelling, *Engineering Fracture Mechanics*, 2013, **102**:118-145.

Mohr D, Henn S, Calibration of stress-triaxiality dependent crack formation criteria: A new hybrid experimental-numerical method, *Experimental Mechanics*, 2007, **47**:805-820.

Mohr D, Marcadet S, Micromechanically-motivated phenomenological Hosford-Coulomb model for predicting ductile fracture initiation at low stress triaxialities, *International Journal of Solids and Structures*, 2015, **67-68**:40-55.

Mordike B L, Ebert T, Magnesium, properties, applications, potential, *Material Science and Engineering A*, 2001, **302**:37-45.

Nashon K, Xue Z, A modified Gurson model and its application to punch-out experiments, *Engineering Fracture Mechanics*, 2009, **76**(8):997-1009.

Nemcko M J, Wilkinson D S, Impact of microstructures on void growth and linkage in pure magnesium, *International Journal of Fracture*, 2016, **200**:31-47.

Nielson K L, Tvergaard V, Ductile shear failure or plug failure of spot welds modelled by modified Gurson model, *Engineering Fracture Mechanics*, 2010, **77**(7):1031-1047.

Noder J, Characterization and simulation of warm forming of 6xxx and 7xxx series aluminum alloys, M.Sc. thesis, University of Waterloo, 2017.

Oyane M, Sato T, Okimoto K, Shima S, Criteria for ductile fracture and their applications, *Journal of Mechanical Working Technology*, 1980, **4**:65-81.

Papasidero J, Doquet V, Mohr D, Ductile fracture of aluminum 2024-T351 under proportional and non-proportional multi-axial loading: Bao-Wierzbicki results revisited, *International Journal of Solids and Structures*, 2015, **69-70**:459-474.

Pardoen T, Hutchinson J, An extended model for void growth and coalescence, *Journal of Mechanics and Physics of Solids*, 2000, **48**:2512-2567.

Park N, Huh H, Lim S J, Lou Y, Kang Y S, Seo M H, Fracture-based forming limit criteria for anisotropic materials in sheet metal forming, *International Journal of Plasticity*, 2017, **96**:1-35.

Peirs J, Verleysen P, Degrieck J, Novel technique for static and dynamic shear testing of Ti6Al4V sheet. *Experimental Mechanics*, 2012, **52**:729-741.

Piao K, Chung K, Lee M G, Wagoner R H, Twinning-slip transitions in Mg AZ31B, *Metallurgical and Materials Transactions A*, 2012, **43**:3300-3313.

Plunkett B, Cazacu O, Barlat F, Orthotropic yield criteria for description of the anisotropy in tension and compression of sheet metals, *International Journal of Plasticity*, 2008, **24**:847-866.

Qiao H, Agnew S R, Wu P D, Modeling twinning and detwinning behavior of Mg alloy ZK60A during monotonic and cyclic loading, *International Journal of Plasticity*, 2015, **65**:61-84.

Qiao H, Guo X Q, Hong S G, Wu P D, Modeling of {10-12}-{10-12} secondary twinning in pre-compressed Mg alloy AZ31, *Journal of Alloys and Compounds*, 2017, **725**:96-107.

Rahmaan T, Abedini A, Butcher C, Pathak N, Worswick M J, Experimental investigation of strain rate effect on fracture characteristics of DP600 and AA5182-O sheet metal alloys under shear loading, *International Journal of Impact Engineering*, 2017, **108**:303-321.

Ray A K, Wilkinson D S, The effect of microstructure on damage and fracture in AZ31B and ZEK100 magnesium alloys, *Materials Science and Engineering A*, 2016, **658**:33-41.

Rice J, Tracey D, On the ductile enlargement of voids in triaxial stress fields, *Journal of Mechanics and Physics of Solids*, 1969, **17**:201-217.

Roth C C, Mohr D, Ductile fracture experiments with locally proportional loading histories, *International Journal of Plasticity*, 2016, **79**:328-354.

Rousselier and Lou, A fully coupled void damage and Mohr-Coulomb based ductile fracture model in the framework of a reduced texture methodology, *International Journal of Plasticity*, 2014, **55**:1-24.

Safaei M, Zang S, Lee M, Waele W D, Evaluation of anisotropic constitutive models: Mixed anisotropic hardening and non-associated flow rule approach, *International Journal of Mechanical Sciences*, 2013, **73**:53-68.

Safaei M, Constitutive modelling of anisotropic sheet metals based on a non-associated flow rule, PhD thesis, 2013, Ghent University.

Scales M, Tardif N, Kyriakides S, Ductile fracture of aluminum alloy tubes under combined torsion and tension, *International Journal of Solids and Structures*, 2016, **97-98**:116-128.

Sinclair C W, Martin G, Local plastic strain inhomogeneity in a ZEK100 alloy, *MATEC Web of Conferences* 2013, 7, 01005.

Staroselsky A, Anand L, A constitutive model for hcp materials deforming by slip and twining: application to magnesium alloy AZ31B, *International Journal of Plasticity*, 2003, **19**:1843-1864.

Steglich D, Tian X, Bohlen J, Kuwabara T, Mechanical testing of thin sheet magnesium alloys in biaxial tension and uniaxial compression, *Experimental Mechanics*, 2014, **54**:1247-1258.

Steglich D, Tian X, Besson J, Mechanism-based modelling of plastic deformation in magnesium alloys, *European Journal of Mechanics A/Solids*, 2016, **55**:289-303.

Stoughton T B, A non-associated flow rule for sheet metal forming, *International Journal of Plasticity*, 2002, **18**:687-714.

Stoughton T B, Yoon J W, Review of Drucker's postulate and the issue of plastic instability in metal forming, *International Journal of Plasticity*, 2006, **22**:391-433.

Stoughton T B, Yoon J W, Anisotropic hardening and non-associated flow in proportional loading of sheet metals, *International Journal of Plasticity*, 2009, **25**:1777-1817.

ten Kortenaar, Failure characterization of hot formed boron steels with tailored mechanical properties, M.Sc. Thesis, 2016, University of Waterloo.

Tuninetti V, Gilles G, Milis O, Pardoen T, Habraken A M, Anisotropy and tension-compression asymmetry modeling of the room temperature plastic response of Ti-6Al-4V, *International Journal of Plasticity*, 2015, **67**:53-68.

Tutyshkin N, Muller W H, Wile R, Zapara M, Strain-induced damage of metals under large plastic deformation: theoretical framework and experiments, *International Journal of Plasticity*, 2014, **59**:133-151.

Tvergaard V, Needleman A, Analysis of the cup-cone fracture in a round tensile bar, *Acta Metallurgica*, 1984, **32**:157-169.

Ulacia I, Dudamell N V, Galvez F, Yi S, Perez-Prado M T, Hurtado I, Mechanical behavior and microstructural evolution of a Mg AZ31 sheet at dynamic strain rates, *Acta Materialia*, 2010, **58**:2988-2998.

Williams B W, Boyle K P, Characterization of anisotropic yield surfaces for titanium sheet using hydrostatic bulging with elliptical dies, *International Journal of Mechanical Sciences*, 2016, **114**:315-329.

Yoon J W, Barlat F, Dick R E, Chung K, Kang T J, Plane stress yield function for aluminum alloy sheets, part II: FE formulation and its implementation, *International Journal of Plasticity*, 2004, **20**:495-522.

Yoon J W, Barlat F, Dick R E, Karabin M E, Prediction of six or eight ears in a drawn cup based on a new anisotropic yield function, *International Journal of Plasticity*, 2006, **22**:174-193.

Zarandi F, Yue S, Magnesium sheet; challenges and opportunities, magnesium alloys, design, processing and properties, Frank Czerwinski (Ed), 2011.

Zhang S, Lou Y, Yoon J W, Finite element formulation of a general asymmetrical yield function for pressure sensitive metals, *Procedia Engineering*, 2017, **207**:215-220.

Appendix A: **Abedini A, Butcher C, Nemcko M J, Kurukuri S, Worswick M J, Constitutive characterization of a rare-earth magnesium alloy sheet (ZEK100-O) in shear loading: studies of anisotropy and rate sensitivity,** *International Journal of Mechanical Sciences*, **2017, 128-129:54-69.**

Accessible through the link below as well as the University of Waterloo's Institutional Repository (UW Space)

http://www.sciencedirect.com/science/article/pii/S0020740316308621

Appendix B: **Abedini A, Butcher C, Worswick M J, An evolving non-associative anisotropic-asymmetric plasticity model for magnesium alloys,** *Submitted for possible publication***, 2017.**

Accessible through the University of Waterloo's Institutional Repository (UW Space)

Appendix C: **Abedini A, Butcher C, Worswick M J, Fracture characterization of rolled sheet alloys in shear loading: Studies of specimen geometries, anisotropy, and rate sensitivity,** *Experimental Mechanics***, 2017, 57:75-88.**

Accessible through the link below as well as the University of Waterloo's Institutional Repository (UW Space)

https://link.springer.com/article/10.1007/s11340-016-0211-9

Appendix D: **Abedini A, Butcher C, Worswick M J, Experimental fracture characterization of an anisotropic magnesium alloy sheet in proportional and non-proportional loading conditions,** *Submitted for possible publication***, 2017.**

Accessible through the University of Waterloo's Institutional Repository (UW Space)

Appendix E: Additional Publications Stemming from This Research

Abedini A, Butcher C, Rahmaan T, Worswick M J, Evaluation and calibration of anisotropic yield criteria in shear loading: Constraints to eliminate numerical artefacts, *International Journal of Solids and Structures*, 2017, DOI: http://dx.doi.org/10.1016/j.ijsolstr.2017.06.029.

Rahmaan T, Abedini A, Zhou P, Butcher C, Worswick M J, High strain rate constitutive characterization of AA7075-T6, AA7xxx-T76, and AA6013-T6 sheet metal alloys, under preparation.

Nemcko M J, Zhumagulov A, Abedini A, Butcher C, Worswick M J, Experimental and numerical investigation on anisotropic plasticity of AA6063-T6 aluminum extrusions, under preparation.

Butcher C, Abedini A, On the path dependence of proportional failure *loci*: Issues of coaxiality and non-uniqueness in combined tension and shear stress states, Submitted to the *International Journal of Solids and Structures*, 2017.

Butcher C, Abedini A, Shear confusion: Identification of the appropriate equivalent strain in simple shear using logarithmic strain measure, *International Journal of Mechanical Sciences*, 2017, DOI: 10.1016/j.ijmecsci.2017.10.005.

Abedini A, Butcher C, Worswick M J, Characterization of evolving plastic anisotropy and asymmetry of a rare-earth magnesium alloy sheet by means of a non-associated flow rule, Proceedings of *XIV International Conference on Computational Plasticity (ComPlas)*, 2017, 656-661.

Rahmaan T, Abedini A, Butcher C, Pathak N, Worswick M J, Experimental investigation of strain rate effect on fracture characteristics of DP600 and AA5182-O sheet metal alloys under shear loading, *International Journal of Impact Engineering*, 2017, 108:303-321.

Abedini A, Butcher C, Rahmaan T, Worswick M J, Universal constraints and numerical issues associated with the calibration of anisotropic yield criteria in shear loading, Proceedings of 16th *Conference of Plasticity*, 2017, Puerto Vallarta, Mexico.

Nemcko M J, Abedini A, Butcher C, Wu P, Worswick M J, Microstructural and numerical investigation on the shear response of a rare-earth magnesium alloy sheet, *Magnesium Technology*, 2017, 477-482.

Abedini A, Butcher C, Worswick M J, Williams B, Skszek T, Kuwabara T, Anisotropic constitutive response of a rare-earth magnesium alloy sheet: Characterization of yield *locus* evolution, Proceedings of *12th NUMIFORM Conference*, 2016, Troyes, France.

Abedini A, Butcher C, Worswick M J, Skszek T, Constitutive response of a rare-earth magnesium alloy sheet in monotonic and cyclic loadings, Proceedings of *24th ICTAM Conference*, 2016.

Abedini A, Butcher C, Worswick M J, Skszek T, Experimental investigations of plasticity and fracture of a rare-earth magnesium alloy sheet, Proceedings of *15th Conference of Plasticity*, 2016, Big Island, USA.

Rahmaan T, Abedini A , Butcher C, Worswick M J, Effect of strain rate on shear properties and fracture characteristics of DP600 and AA5182-O sheet metal alloys, Proceedings of *DYMAT Conference*, 2015, Lugano, Switzerland.

Abedini A, Butcher C, Anderson D, Worswick M J, Skszek T, Fracture characterization of automotive alloys in shear loading, *SAE International Journal of Materials and Manufacturing*, 2015, 8(3).